Patient-Specific Midbrain Organoids with CRISPR Correction Recapitulate Neuronopathic Gaucher Disease Phenotypes and Enable Evaluation of Novel Therapies

Yi Lin[1], Benjamin Liou[1], Venette Fannin[1], Stuart Adler[1], Christopher N. Mayhew[2,3], Jason E. Hammonds[2,4], Yueh-Chiang Hu[2,5], Jason Tchieu[2,6], Wujuan Zhang[7], Xueheng Zhao[2,7], Rebecca L. Beres[7], Kenneth DR. Setchell[2,7], Ahmet Kaynak[8], Xiaoyang Qi[2,8], Ricardo A. Feldman[9], Ying Sun[1,2*].

[1] Division of Human Genetics, Cincinnati Children's Hospital Medical Center, Cincinnati, OH

[2] Department of Pediatrics, University of Cincinnati College of Medicine, Cincinnati, OH

[3] Pluripotent Stem Cell Facility & Developmental Biology, Cincinnati Children's Hospital Medical Center, Cincinnati, OH

[4] Division of Infectious Diseases, Cincinnati Children's Hospital Medical Center, Cincinnati, OH

[5] Transgenic Animal and Genome Editing Facility, Cincinnati Children's Hospital Medical Center, Cincinnati, OH

[6] Division of Developmental Biology, Cincinnati Children's Hospital Medical Center, Cincinnati, OH

[7] Division of Pathology and Laboratory Medicine, Cincinnati Children's Hospital Medical Center, Cincinnati, OH

[8] Division of Hematology/Oncology, Department of Internal Medicine, University of Cincinnati, College of Medicine, Cincinnati, OH

[9] Department of Microbiology and Immunology, University of Maryland School of Medicine, Baltimore, MD

*Corresponding author. Division of Human Genetics, Cincinnati Children's Hospital Medical Center, S Building Rm. 4.216, 3333 Burnet Ave, Cincinnati, OH 45229, United States. E-mail: Ying.Sun@cchmc.org

Abstract

Neuronopathic Gaucher disease (nGD) is a lysosomal storage disorder caused by *GBA1* mutations, leading to defective acid β-glucosidase (GCase) and accumulation of glycosphingolipid substrates, causing inflammation and neurodegeneration. Patients with nGD manifest severe neurological symptoms, but current animal models fail to fully recapitulate human condition, posing a major barrier to the development of effective therapies targeting the brain. To bridge this gap, we have developed midbrain-like organoids (MLOs) from human induced pluripotent stem cells (hiPSCs) of nGD patients with *GBA1*$^{L444P/P415R}$ and *GBA1*$^{L444P/RecNcil}$ mutations to model nGD brain pathogenesis. These nGD MLOs exhibited GCase deficiency, resulting in diminished enzymatic function, accumulation of lipid substrates, widespread transcriptomic changes, and impaired dopaminergic neuron differentiation, mirroring nGD pathology. *GBA1* mutation correction mediated by CRISPR/Cas9 restored GCase activity, normalized lipid substrate levels, and rescued dopaminergic neuron function, confirming the causal role of *GBA1* mutations during early brain development. Using this novel platform, we further evaluated therapeutic strategies, including SapC-DOPS nanovesicles delivering GCase, AAV9-GBA1 gene therapy, and substrate reduction therapy with GZ452, a glucosylceramide synthase inhibitor currently under clinical investigation. These treatments either restored GCase activity, reduced lipid substrate accumulation, improved autophagic and lysosomal abnormalities, or ameliorated dysregulated genes involved in neural development. These patient-specific, 3D neural models offer a transformative, physiologically relevant platform for unravelling disease mechanisms and accelerating the discovery of therapies for patients with nGD.

52 **Introduction**

53 Gaucher disease (GD) is a lysosomal storage disorder caused by *GBA1* mutations, which impair
54 acid β-glucosidase (GCase). Defective GCase leads to accumulation of its glycosphingolipid
55 substrates, glucosylceramide (GluCer) and glucosylsphingosine (GluSph), triggering
56 inflammation and neurodegeneration. GD affects 1/450 in Ashkenazi individuals and 1/50,000
57 globally [1]. There are three GD types: Type 1 present mainly visceral symptoms and is not life-
58 threatening [1]. while neuronopathic GD (nGD, Types 2 and 3) involves severe neurological
59 manifestations. Type 2 patients typically die by age 2, indicating early central nervous system
60 (CNS) defects [2,3].

61

62 Current knowledge of brain pathogenesis in nGD is limited to a few postmortem brain analyses
63 showing prominent neuronal loss and astrogliosis in the midbrain [4-6]. GD mouse models, including
64 GCase knockout, irreversible GCase inhibitor conduritol B-epoxide (CBE) induced mouse models,
65 double transgenic mutant model harboring both *Gba1* and Saposin C mutations (Saposin C is the
66 activator of GCase), have been widely used to study disease pathogenesis and therapies [7-12]. These
67 models replicate neuronal loss and astrogliosis [4-6,8,13], but have limitations. The knockout and CBE-
68 induced models lack *GBA1* mutations, and the double transgenic model has a second gene that
69 may change the GD phenotype, and knock-in models fail to mimic human phenotypes [10,14]. For
70 example, mice with the $Gba1^{L444P/L444P}$ or $Gba1^{D409H/D409H}$ mutations show no neuronopathic
71 disease despite <10% of residual GCase activity [10,14-16]. These constraints highlight the need for
72 physiologically relevant human nGD models.

73

74 Brain organoids derived from human induced pluripotent stem cells (hiPSC) emerged as a

75 powerful 3D model to study brain development and CNS diseases [17]. Unlike 2D monolayer neural
76 cells, brain organoids contain diverse neural and glial cell types arranged in 3D comprising
77 subventricular zone and multiple organized cellular layers that more closely represents the spatial
78 architecture of the human brain [18]. They have been used to study neurodegenerative and lysosomal
79 diseases, including Parkinson's disease (PD), Alzheimer's disease, and Sandhoff disease [19-23]. A
80 brain organoid derived from hiPSCs of a healthy individual with *GBA1* knockout and α-synuclein
81 overexpression exhibited characteristic PD markers [24]. However, this model lacks patient-specific
82 *GBA1* mutations needed for clinical relevance. To develop a relevant model, we developed novel
83 midbrain organoids from nGD patients with *GBA1* mutations, a model not yet well studied.
84
85 The midbrain region is prominently affected in nGD [4-6]. Patients with nGD often exhibit impaired
86 vertical gaze and movement disorders. These symptoms correlate with midbrain involvement due
87 to the sensitivity of this region to neuroinflammatory and degenerative processes [4,25]. Both human
88 and mouse studies indicate that the midbrain shows prominent substrate accumulation compared
89 with other brain regions, suggesting it is particularly susceptible to pathological burden in GD
90 midbrain [4,26-28]. To model the midbrain-specific disease, we derived midbrain-like organoids
91 (MLOs) from Type 2 patient-derived hiPSCs carrying either *GBA1*$^{L444P/P415R}$ or *GBA1*$^{L444P/RecNcil}$
92 mutations. These GD MLOs showed reduced GCase activity, lipid substrate accumulation,
93 transcriptomic alterations, and impaired dopaminergic neuron differentiation. CRISPR/Cas9-
94 mediated correction of *GBA1* mutation confirmed the causal role of *GBA1* mutations in these
95 phenotypes and mitigated disease phenotypes. To explore therapeutic potential, we tested three
96 emerging treatments in GD MLOs: CNS accessible enzyme therapy (SapC-DOPS-GCase), gene
97 therapy (AAV9-GBA1) and substrate reduction therapy (GZ452). Our results demonstrate the

98 utility of patient-derived MLOs for studying nGD pathogenesis and advance drug development.

99

100

Materials and Methods

Maintenance of hiPSCs and generation of MLOs

Three hiPSCs lines (WT-75.1, GD2-1260 and GD2-10-257) generated previously [29,30] (Supplementary Table 1) were maintained in mTeSR1 complete medium (StemCell) on six-well plates coated with Vitronectin (1:100 diluted in DPBS, 1 mL/well, incubated at RT for 1 hour). HiPSCs at ~70% confluency were treated and replated at 1:20 to 1:60 ratios, with optional 10 μM ROCK inhibitor (Y-27632, StemCell) for survival. All hiPSC lines were authenticated using short tandem repeat (STR) profiling and were verified as mycoplasma-free.

MLO generation method was modified based on published protocol [31,32]. Briefly, hiPSCs were pretreated with 50 μM Y-27632 for 1 hour, dissociated with Accutase (Millipore-Sigma) into singlets, centrifuged (200 × g, 5 minutes), and resuspended in embryoid body (EB) medium (EBM; consisting of DMEM/F12, 20% KnockOut Serum Replacement (KSR), 1% penicillin/streptomycin, GlutaMAX, NEAA, 55 μM β-mercaptoethanol, 1 μg/mL heparin, 3% FBS, 4 ng/mL bFGF, 1× CEPT). For each organoid, 1.2~1.5 × 10^4 hiPSC cells were seeded in 100 μL EBM per well in ultra-low attachment (ULA) U-bottom 96-well plates, centrifuged at 500 × g for 3 minutes, and incubated at 37°C, 5% CO_2; on day 2, 150 μL EBM with 4 ng/mL bFGF (no ROCK inhibitor) was added. Once the EBs grow to 400 to 475 μm in size, they were transferred to a new ULA 96-well plate with 125 μL brain organoid generation medium (BGM, consisting of 50% DMEM/F12, 50% Neurobasal, 1× N2, 1× B27 without vitamin A, 1% penicillin/streptomycin, 1% GlutaMAX, 1% NEAA, 55 μM β-mercaptoethanol, 1 μg/mL heparin) supplemented with dual SMAD inhibitors (SMADi: 2 μM dorsomorphin, 2 μM A83-01, 3 μM CHIR99021, 1 μM IWP2), refreshed every other day until day 11. On day 7 or 8, mesencephalic floor plate induction was

124 initiated by adding 125 μL BGM containing 1× SMADi, 100 ng/mL FGF8, and 2 μM SAG until
125 day 16. On day 11, four EBs were transferred to one well of ultra-low attachment 24-well plates
126 with 500 μL BGM-MLOs induction medium, consisting of BGM with 100 ng/mL FGF8, 2 μM
127 SAG, 200 ng/mL laminin, 2.5 μg/mL insulin, 2% Growth Factor Reduced (GFR) Matrigel, and
128 refreshed with Matrigel on day 14. On day 16, three MLOs per well were transferred to ultra-low
129 attachment 6-well plates in brain organoid maturation medium (BGM-BMM), consisting of BGM
130 with 10 ng/mL BDNF, 10 ng/mL GDNF, 200 μM ascorbic acid, 125 μM db-cAMP, 1% GFR
131 Matrigel, cultured on an orbital shaker (100 rpm) to reduce spontaneous fusion with medium
132 changes every 3 days. Starting at day 30, GFR Matrigel was removed, and brain organoids were
133 cultured solely in BGM medium till the date of analysis.
134

135 **Immunostaining and image analysis of sectioned MLOs**

136 Organoids were washed with 1xDPBS and fixed in 4% paraformaldehyde (PFA) overnight at 4°C.
137 After washing with PBS-T (1 x DPBS with 0.1% Tween 20), organoids were cryoprotected in 30%
138 sucrose solution until fully equilibrated. Samples were then embedded in gelatin solution (7.5%
139 gelatin, 10% sucrose in 1xDPBS) at 37°C for 1 hour, snap-frozen in a dry ice/ethanol slurry, and
140 stored at -80°C. Cryosectioning was performed to obtain 16-μm-thick sections. For
141 immunofluorescence, sections were air-dried and outlined with a hydrophobic PAP pen before
142 blocked with 5% normal goat serum in PBS-T for 1 hour, incubated overnight with primary
143 antibodies (Supplementary Table 1) in primary antibody dilution buffer (PBS-T with 5% BSA and
144 0.05% sodium azide), and followed by secondary antibodies (Alexa Fluor® conjugates) for 1 hour
145 at room temperature. Slides were washed, stained with DAPI solution (0.2 μg/mL), mounted with
146 Antifade Mounting Medium (VECTASHIELD®, H-1000-10), and imaged at 10× magnification

147 for whole organoid scans or 60× magnification for detailed cellular analysis using a fluorescence
148 confocal microscope (Nikon Eclipse *Ti*) (Nikon, Tokyo, Japan) to assess neuronal organization of
149 MLOs. The morphologies of neurons, astrocytes, and colocalization analysis were performed by
150 taking multi-layer stacking (Z-stack) images under 60× oil immersion objective lens.
151 Quantitative immunofluorescence analyses (e.g., cell counts for FOXP1+, FOXG1+, SOX2+ and
152 Ki67+ cells, as well as marker colocalization) were performed using ImageJ (NIH) on at least 3 -
153 5 randomly selected non-overlapping fields of view (FOVs) per organoid section, with a minimum
154 of 3 organoids per differentiation batch. Each FOV was imaged at consistent magnification (60x)
155 and z-stack depth to ensure comparable sampling across conditions. Data from individual FOVs
156 were first averaged within each organoid to obtain an organoid-level mean, and then biological
157 replicates (independent differentiations, $n \geq 3$) were averaged to generate the final group mean ±
158 SEM.
159

160 **Genome editing patient iPSC clones**

161 The iPSC line (GD2-1260) used for gene correction was derived from fibroblasts obtained from a
162 GD Type 2 patient carrying compound heterozygous *GBA1* mutations (P415R/L444P) [29]. A guide
163 (g) RNA was designed to target SpCas9-mediated double strand break introduction proximal to
164 the L444P mutation (*GBA1* mutation at nt14446, T>C) in GD2-1260. Oligonucleotides
165 (caccGAAGAACGACCCGGACGCAG and aaacCTGCGTCCGGGTCGTTCTTC; overhangs in
166 lower case; target mutation site underlined; IDT) transcribing the sgRNA target sequence were
167 annealed and cloned via BbsI restriction digest into plasmid pX458M that contains a U6 promoter-
168 driven sgRNA and a SpCas9-2A-EGFP expression cassette. The pX458M plasmid is modified
169 from the pX458 plasmid (addgene #48138) [33] and carries an optimized sgRNA scaffold [34]. The

170 targeting activity of this plasmid was validated by T7E1 assay using 293 cells. GD2-1260 cells
171 were transfected with pX458M and a phosphorothioate-modified single stranded oligonucleotide
172 (ssODN; IDT) donor template using TransIT-LT1 (Mirus). The ssODN (Supplementary Figure 1A)
173 was designed to introduce the desired wildtype *GBA1* sequence flanked by homology arms to the
174 targeted genomic region. The ssODN was also designed to contain silent mutations to prevent
175 retargeting by SpCas9 and to introduce a BtgI restriction site to facilitate identification of targeted
176 clones. Forty-eight hours post-transfection, GFP-positive cells were isolated by FACS and replated
177 at cloning density (250-500 cells/well of a 6 well matrigel-coated plate). Replated cells were
178 cultured for 4 days in mTeSR1 containing 10% CloneR (StemCell Technologies), using the
179 manufacturer's recommended protocol. Cells were subsequently fed daily with mTeSR1 for an
180 additional 9 days before colonies were manually harvested and expanded for genotyping. Primers
181 VS4247 (gtgcgtaactttgtcgacagtcc) and VS4249 (ctgagagtgtgatcctgccaag) were used to PCR
182 amplify the targeted *GBA1* genomic region and products were subjected to BtgI digestion to
183 identify putative edited clones. Selected clones were subsequently confirmed by Sanger
184 sequencing. This gene editing strategy is expected to also target the *GBA1* pseudogene due to the
185 identical target sequence which limits the gene correction on certain mutations (e.g., P415R) [35,36],
186 but the chance to target other off-targets is low due to low off-target scores ranked based on the
187 MIT Specificity Score analysis [37].
188

189 **SapC-DOPS-fGCase treatment of MLOs**

190 As previously described [38,39], SapC-DOPS nanovesicles were formulated by combining saposin C
191 (SapC) with dioleoylphosphatidylserine (DOPS) to encapsulate either recombinant human acid β-
192 glucosidase (fGCase, Freeline Therapeutics) or fluorescent CellVue Maroon (CVM) for uptake

193 studies. The SapC-DOPS-fGCase complex was prepared at a final concentration of 0.6 μg/mL
194 fGCase and added to the BGM culture medium of MLOs derived from WT-75.1, GD2-1260, and
195 GD2-10-257 hiPSC lines. To assess nanovesicle uptake, WT-75.1 MLOs at week 13 were co-
196 cultured with SapC-DOPS-CVM for 48 hours, followed by confocal imaging to confirm
197 internalization of the fluorescent CVM within the organoids.
198
199 For enzyme delivery and therapeutic evaluation, MLOs were treated with SapC-DOPS-fGCase or
200 SapC-DOPS alone (control) for a 48-hour period to assess uptake and enzyme activity. For long-
201 term treatment efficacy, MLOs were treated for two weeks before evaluating therapeutic efficacy.
202 During treatment, MLOs were maintained in BGM media containing nanovesicles and were
203 replaced every 3 days to ensure consistent exposure. Post-treatment, MLOs were harvested for
204 confocal imaging, enzymatic assays, and biochemical analyses to assess GCase activity, protein
205 expression, and correction of GD phenotypes.
206
207 **AAV injection into MLOs**
208 Transfer vector of AAV9-GBA1 virus containing GBA1/GFP expressing cassette (CB-GBA1-
209 IRES-GFP) was packaged in AAV9 capsid at AAVnerGene (Rockville, MD, USA). For the
210 delivery of AAV9-GBA1 gene therapy to MLOs, a precise injection protocol was employed using
211 a nanoliter injector system (World Precision Instruments). MLOs derived from WT-75.1, GD2-
212 1260, and GD2-10-257 hiPSC lines were placed in a dish containing sterile 1 x PBS. A glass pipette
213 connected to a gas injector was lowered into the center of each MLO at a desired depth of 200 to
214 300 μm, as determined by microscopic visualization. A volume of 500 nL (0.5μL) of AAV9-GBA1
215 vector, at a concentration of 3.6×10^{13} vg/mL, was injected into ten sites of MLOs at a volume of

216 50 nL per injection site. The injection glass needle was retracted slowly after completion of the
217 injection to minimize damage and ensure vector distribution. Morphology and viability were
218 assessed post-injection, and MLOs were then maintained in culture for 3 weeks prior to subsequent
219 analyses.
220

221 **Substrate Reduction Therapy treatment of MLOs**

222 For evaluation of the tolerated dose of Substrate Reduction Therapy (SRT), WT-75.1 MLOs were
223 treated with SRT compound GZ452 (AstaTech, P14969), also named GZ-682452, an analogue of
224 venglustat [40], at concentrations of 0.3, 1, 2, and 3 μM starting on day 0 for a period of 6 weeks.
225 MLO size was measured weekly using bright-field microscopy and analyzed with ImageJ software
226 to assess morphological changes. For short-term SRT treatment, 13-week-old GD2-1260 MLO
227 were treated with 300nM GZ452 for 3 weeks, with medium refreshed every 3 days to maintain
228 consistent drug exposure. For long-term SRT treatment, GZ452 treatment at the concentration of
229 300nM was started at the beginning of MLO generation (day 1) and continued for 28 weeks before
230 collection for analysis. Untreated MLOs served as controls.
231

232 **Glycosphingolipids analyses**

233 MLOs were washed with ice-cold PBS and homogenized and sonicated in sterile ddH_2O.
234 Glycosphingolipids were then extracted from tissue homogenates using chloroform/methanol
235 following protocol outlined previously [41]. Aliquots of lipids extracts were processed for GluCer
236 and GluSph quantification by ultra-high-performance chromatography coupled to tandem mass
237 spectrometry (UHPLC-MS/MS) using a Waters Xevo TQ-S Micro triple quadrupole mass
238 spectrometer (Waters, Milford, MA) at CCHMC Clinical Mass Spectrometry Laboratory.

239 Chromatographic separation for GluCer and GluSph was achieved using a XSelect CSH C18 XP
240 Column (100 x 2.1 mm, 2.5 µm, Waters) column. Quantification by LC-MS/MS was operated in
241 the multiple reaction monitoring (MRM) mode, with detection of the transition pair of the
242 individual protonated parent ions of GluCers and daughter ion m/z 264.2. GluSph was measured
243 by monitoring the mass transition m/z 462.3> 282.4. The sphingoid base for all GluCer species
244 analyzed is d18:1. Calibration curves were prepared for C16 GluCer, C18 GluCer, C24 GluCer,
245 and C24:1 GluCer using C18 glucosyl(ß) ceramide-D5 as the internal standard. Quantification of
246 GluCer species with various fatty acid chain lengths was realized by the calibration curve of each
247 species or with the closest fatty acyl chain length. The quantification of GluSph was based on the
248 calibration curve using glucosyl(β) sphingosine-D5 as internal standard. The calibration curve for
249 GluCer and GluSph was 25 pg–10 ng on column. Three QCs at low, medium and high levels (50
250 pg, 0.5 ng and 5.0 ng) were prepared in organic solvent and analyzed along with samples. The
251 GluCer and GluSph levels in MLO were normalized to total MLO protein (mg) that were used for
252 glycosphingolipids analyses. Protein mass was determined by BCA assay and glycosphingolipid
253 was expressed as pmol/mg protein. Additionally, GluSph levels in the culture medium were
254 quantified and normalized to the medium volume (pmol/mL) [42].
255

256 **Measuring Dopamine levels by ELISA**

257 Dopamine levels in MLO culture medium were quantified using the Dopamine ELISA Kit
258 (Abnova) that involves dopamine extraction, acylation and enzymatic conversion before assay.
259 Briefly, MLO culture medium was collected from 4 MLOs cultured in 3 mL BGM medium for 72
260 hours. Dopamine extraction was performed by pipetting 10 µL of standards, controls, and 750 µL
261 of the sample into the extraction plate wells, filling each to 750 µL with deionized water, followed

262 by 25 μL of TE buffer. Shake the covered plate for 60 minutes at room temperature (RT, 20-25°C)
263 at 600 rpm, wash with 1 mL wash buffer twice, then acylate with 150 μL acylation buffer and 25
264 μL acylation reagent for 20 minutes. After washing again, elute with 100 μL hydrochloric acid,
265 and transfer 90 μL of supernatant to the microtiter plate for enzymatic conversion with 25 μL
266 freshly prepared enzyme solution, incubating at 37°C for 2 hours. Then, 100 μL of the converted
267 samples and 50 μL dopamine antiserum were added to the dopamine microtiter strips. The mixture
268 was then incubated overnight at 2-8°C. The strips were then washed and incubated with 100 μL
269 enzyme conjugate for 30 minutes, followed by 100 μL of substrate for 20-30 minutes, and finally,
270 100 μL of stop solution was added. Absorbance was measured at 450 nm within 10 minutes, and
271 dopamine concentrations were calculated using a calibration curve, applying the correction factor
272 (10/500 = 0.02) to adjust and normalize by sample volume.
273

274 **GCase activity assay**

275 GCase enzyme activities in hiPSCs and MLOs were determined fluorometrically with 4-
276 methylumberlliferyl-β-D-glucopyranoside (4MU-Glc) in the presence of the GCase irreversible
277 inhibitor, Conduritol B epoxide (CBE, 2 mM, Millipore, Bedford, MD) as previously described [43].
278 Briefly, hiPSC cell pellet or MLO tissues were homogenized using Precellys Evo
279 Homogenizer/CK Mix beads (Bertin Technologies, France) in 1% sodium taurocholate/1%Triton
280 X-100 (Tc/Tx) solution. GCase enzyme activity was then determined by 4MU-Glc as substrate in
281 0.25% Tc/Tx diluted in 0.1 M citrate phosphate buffer (pH 5.6). Protein concentrations were
282 determined by BCA assay for normalization. The GCase-specific activity was calculated by
283 subtracting non-specific activity (with CBE) from total activity (without CBE) and normalized to
284 total protein mass.

285

286 **Transcriptome analysis of MLOs**

287 Total RNAs were extracted from week 8 MLOs using the RNeasy Mini Kit (Qiagen). Total RNAs
288 (150 to 300 ng), quantified by Qubit (Invitrogen) high-sensitivity spectrofluorometric assay, were
289 poly-A selected and reverse transcribed using Illumina's TruSeq® stranded mRNA library
290 preparation kit (Illumina). Each sample was fitted with one of 96 adapters containing different 8-
291 base molecular barcodes for high-level multiplexing. After 15 cycles of PCR amplification,
292 completed libraries were sequenced on NovaSeq 6000 (Illumina), generating 30 million high-
293 quality 100-base-long paired-end reads per sample. A quality control check on the fastq files was
294 performed using FastQC. Upon passing basic quality metrics, the reads were trimmed to remove
295 adapters and low-quality reads using default parameters in Trimmomatic (Version 0.33). The
296 trimmed reads were then mapped to human reference genome GRCh38 using default parameters
297 with strandness option in Hisat2 (Version 2.0.5), achieving a mapping rate greater than 90%.
298 Transcript or gene abundance was determined using kallisto (Version 0.43.1). A transcriptome
299 index in kallisto was created using Ensembl cDNA sequences for the reference genome. This index
300 was then used to quantify transcript abundance in raw counts and transcript per million (TPM).
301 Differential expression analysis was performed using the R package DESeq2 [44]. Genes with
302 BaseMean ≥ 50, $|\text{fold change}| \geq 2$, p-adj ≤ 0.05 were identified as differentially expressed genes
303 (DEGs). Heatmaps were made using the R package ggplot2. Gene enrichment analysis using
304 cellular component, KEGG pathways, molecular function, and biological process (GO analysis)
305 was performed using DAVID 6.8 [45]. Three MLOs were pooled for each sample and three samples
306 were profiled for each genotype. MLO Sequencing datasets and partially processed results have
307 been deposited to the National Center for Biotechnology Information (NCBI)'s Gene Expression

308 Omnibus (GEO) database (GSE303993).

309

310 **Gene expression analysis by qRT-PCR**

311 Total RNA was isolated from MLO tissue using the RNeasy Kit (Qiagen). Quantitative RT-PCR
312 was carried out as described previously using primers listed in Supplementary Table 1 [46].
313 Housekeeping gene *GAPDH* or *ACTB* was used as internal controls for mRNA quantification.
314 Relative expression of mRNAs was determined by the $2^{-\Delta\Delta}$CT method.

315

316 **Immunoblotting**

317 Immunoblotting was used to detect protein expression in iPSCs and MLOs. Briefly, brain
318 organoids or cells were homogenized in freshly prepared RIPA buffer with protease inhibitors and
319 anti-phosphatase inhibitors using a Precellys Evo Homogenizer (Bertin). The samples were then
320 centrifuged at 12,000 g for 10 min to produce lysate for electrophoresis, membrane transferring,
321 and detection using primary and secondary antibodies indicated in Supplementary Table 1. Semi-
322 quantification of proteins was performed using ImageJ (NIH).

323

324 **Statistical analysis**

325 For comparisons between two groups, data were analyzed using unpaired two-tailed Student's t-
326 tests when the sample size was ≥ 6 per group and normality was confirmed by the Shapiro-Wilk
327 test. When the normality assumption was not met or when sample sizes were small ($n < 6$), the
328 non-parametric Mann-Whitney U test was used instead. For comparisons involving three or more
329 groups, one-way ANOVA followed by Tukey's multiple comparison test was applied when data
330 were normally distributed; otherwise, the non-parametric Dunn's multiple comparison test was

used. Exclusion of outliers was made based on cutoffs of the mean ±2 standard deviations. All statistical analyses were performed using GraphPad Prism 10 software. Exact p-values are reported throughout the manuscript and figures where feasible. A p-value < 0.05 was considered statistically significant.

336 **Results**

337 **Generation and characterization of MLOs derived from hiPSCs**

338 To generate MLOs from iPSCs, healthy hiPSCs were differentiated following a stepwise protocol,
339 neural induction, neuroepithelial expansion, and maturation, adopted with modifications from
340 previous studies [31,32] (Figure 1A). Midbrain specification during development requires appropriate
341 posterior differentiation signals [47,48]. Our protocol used sequential activation/inhibition of critical
342 signaling pathways involved in midbrain specification: Wnt signaling (activated by CHIR99021),
343 BMP signaling (inhibited by dual-SMAD), and FGF signaling (activated by FGF8) (Figure 1A).
344 MLOs were matured and characterized using immunofluorescence, gene expression, and
345 immunoblotting. Week 8 MLOs showed diverse neural cell types, including pan-neurons
346 (Tuj1/NeuN), astrocytes (GFAP), dopaminergic (DA) neurons (FOXA2/TH), and neural
347 progenitor cells (SOX2/Ki67) (Figure 1B). Comparative analysis of forebrain marker FOXG1
348 expression between MLOs and cerebral organoids (COs) showed barely detectable FOXG1 in
349 MLOs (Figure 1C). Quantitative RT-PCR analysis demonstrated a significant increase in
350 midbrain/DA neuron-specific genes (*FOXA2*, *ASCL1*, *LMX1A*, *PLZF*, and *TH*) from week 3 and
351 week 8 MLOs, demonstrating the midbrain identity of these organoids. Expression of glial-specific
352 genes (*GLAST*, *S100B*) increased over time, while pluripotency markers (*SOX2*, *NANOG*, *OCT4*)
353 were downregulated, suggesting progressive neural differentiation (Figure 1D). Immunoblot
354 further validated hiPSCs differentiation into MLOs by expression of neuronal (Tuj1, MAP2), DA
355 neuronal (TH), and glial (GFAP, S100B) markers at week 8, with reduced Sox2 expression in
356 MLOs versus hiPSCs (Figure 1E). Together, these results confirm the successful generation of
357 MLOs with midbrain-like cellular composition and molecular identities.

358

359 **GCase deficiency in GD MLOs leads to glycosphingolipids accumulation and altered**

360 **transcriptomic profiling**

361 To model nGD and investigate the impact of GCase deficiency on MLOs, we generated GD MLO
362 using the GD2-1260 hiPSC line derived from GD Type 2 patient harboring *GBA1*$^{L444P/P415R}$,
363 compound heterozygous mutations, using same protocol in Figure 1 (Figure 2) [29]. Midbrain
364 identity of GD MLOs was confirmed by TH/FOXA2 expression (Figure 3). Immunoblot showed
365 an approximately 85% reduction in GCase protein levels in week 8 GD2-1260 MLOs versus WT-
366 75.1 MLOs (Figure 2A). Consistent with reduced GCase protein, GCase activity decreased to 14.2%
367 in GD2-1260 hiPSCs and 15.0% in GD2-1260 MLOs vs. WT-75.1 ($p < 0.001$; Figure 2B). Bright-
368 field imaging at weeks 4, 8, and 15 showed no difference on overall MLOs appearance between
369 WT-75.1 and GD2-1260 MLOs (Figure 2C). MLO size measurements revealed a trend toward
370 smaller GD2-1260 MLOs versus WT-75.1 at week 8, though not statistically significant (Figure
371 2D).

372

373 Loss of GCase function in GD disrupts glycosphingolipids metabolism, a primary pathogenic
374 factor in nGD [49]. Mass spectrometry analysis demonstrated significant glycosphingolipid substrate
375 accumulation in GD2-1260 MLOs. At week 15, total glucosylceramide (GluCer) level was
376 elevated approximately 1.39-fold in GD2-1260 MLOs compared to WT-75.1 MLOs ($p < 0.05$;
377 Figure 2E). GluCer analysis revealed marked accumulation of species 18:0 and 16:0, particularly
378 brain predominant species (18:0) in GD2-1260 MLOs, while other species remained largely
379 unchanged (Figure 2F, Supplementary Figure 2). Similarly, glucosylsphingosine (GluSph), a toxic
380 lipid associated with nGD [4,40,50], was significantly elevated approximately 3.3-fold and 5.6-fold in
381 GD2-1260 MLOs at weeks 15 and 28, respectively, versus WT-75.1 controls (Figure 2G,
382 Supplementary Figure 2). These findings indicate profound lipid substrates dysregulation in

383 GCase-deficient GD MLOs, consistent with the biochemical hallmark of GD.

384

385 To explore the transcriptomic consequences of GCase deficiency, we performed bulk RNA
386 sequencing on week 8 MLOs, when DA neurons maturation and GD phenotypes were evident.
387 Principal component analysis (PCA) revealed distinct clustering of WT-75.1 and GD2-1260 MLOs,
388 with the first principal component accounting for 53% of the variance, indicating significant
389 transcriptomic differences between two genotype groups (Figure 2H). An MA plot identified 1,429
390 differentially expressed genes (DEGs) in GD2-1260 MLOs compared to WT-75.1, with 664 genes
391 upregulated and 765 genes downregulated. GO analysis of these DEGs revealed significant
392 enrichment in pathways including cAMP, PI3K-AKT, and WNT signaling that control the nervous
393 system development, axon guidance, and neuron differentiation (Figure 2J). KEGG analysis
394 similarly identified dysregulation in neural signaling pathways, synaptic transmission, and
395 lysosomal function (Figure 2K). The heatmap of these DEGs elucidated specific gene expression
396 changes within key pathways (Figure 2L-2O), including WNT signaling (Figure 2L) [30], anterior-
397 posterior brain specification (Figure 2M), neuronal function (Figure 2N), and lysosome-
398 phagosome (Figure 2O) in GD2-1260 MLOs, with many genes exhibiting upregulation or
399 downregulation consistent with nGD pathology.

400

401 Collectively, these results demonstrate that *GBA1* mutation in GD MLOs leads to reduced enzyme
402 activity, causes lipid substrate accumulation, and alters transcriptomic profiles, particularly in
403 neural development, signaling, and lysosomal function. These findings provide insights into nGD
404 mechanism and support MLOs as a model for studying nGD.

405

406 **Skewed specification of midbrain patterning and dopaminergic neuron differentiation in GD**
407 **MLOs**

408 Building on the molecular and transcriptomic hallmarks of GCase deficiency observed in nGD
409 MLOs (Figure 2), we next investigated the impact on midbrain patterning and dopaminergic
410 neuron differentiation (Figure 3). Firstly, RNA sequencing data revealed elevated FOXG1 and
411 PAX6, and reduced FOXP1 mRNAs in GD2-1260 MLOs versus WT-75.1 MLOs at week 8 (Figure
412 2M, Figure 3A). These genes are fate-determining regulators in controlling proper anterior-
413 posterior neural patterning [51-53]. Immunofluorescence confirmed reduced FOXP1+ and increased
414 FOXG1+ cell counts in GD2-1260 MLOs (Figure 3B, 3C). About 11.6% cells were FOXP1+
415 FOXG1+ cells in GD2-1260 MLOs, but they were barely seen in WT-75.1 MLOs. These results
416 indicate a significant disruption in expression of genes involved in forebrain and midbrain
417 patterning in GD MLOs.

418

419 The skewed specification of midbrain patterning may contribute to dysregulated dopaminergic
420 neuron development in GCase-deficient GD MLOs (Figure 3). There were clear differences in the
421 expression of midbrain-specific markers between WT-75.1 and GD2-1260 organoids at week 6
422 (Figure 3D). In WT-75.1 MLOs, FOXA2 (a midbrain progenitor marker) and TH (dopaminergic
423 neuron marker) were strongly expressed and co-localized (Figure 3D, 3E), indicating normal
424 midbrain patterning. In contrast, GD2-1260 MLOs showed markedly reduced FOXA2+, TH+ and
425 FOXA2+TH+ cells (Figure 3D, 3E). Quantitative analysis confirmed the significant reduction of
426 midbrain progenitor markers (*ASCL1*, *TH*, *FOXA2*, and *PLZF*) in GD2-1260 MLOs versus WT-
427 75.1 (Figure 3F). At week 8, expression levels of *ASCL1*, *TH*, *FOXA2*, and *PLZF* were
428 significantly reduced by approximately 71.0%, 44.4%, 90.0% and 69.8%, respectively, indicating

429 a profound impairment in midbrain progenitor specification due to GCase deficiency. Immunoblot
430 showed ~77.5% and ~66.5% reductions in TH and FOXA2, respectively, and a 27.7% increase in
431 MAP2 in GD2-1260 versus WT-75.1 MLOs (Figure 3H). Dopaminergic function was determined
432 by measuring dopamine levels in the culture medium (Figure 3I). Dopamine levels in week 12
433 MLOs culture medium (72 hours culture) were 76.0% ($p < 0.001$) lower in GD2-1260 MLOs
434 versus WT-75.1 MLOs, confirming impaired dopaminergic function in GD MLOs.
435
436 These results indicate that GCase deficiency leads to skewed midbrain patterning and
437 dopaminergic neuron differentiation, underscoring the critical role of GCase in midbrain
438 development, as revealed for the first time, using patient iPSC-derived brain organoids.
439
440 **CRISPR/Cas9-mediated *GBA1* mutation correction rescues disease phenotypes in GD MLOs**
441 GD is an autosomal recessive disorder. Individuals who are carriers or heterozygous for *GBA1*
442 mutations typically do not exhibit disease phenotypes [1]. To determine whether correction of the
443 *GBA1* mutation could rescue GD phenotypes in GD MLOs, we used CRISPR/Cas9 technology to
444 correct the L444P mutation in GD2-1260 hiPSCs ($GBA1^{L444P/P415R}$) and generated isogenic iso-
445 GD2-1260 hiPSCs with a heterozygous genotype of $GBA1^{WT/P415R}$ (Figure 4A; Supplementary
446 Figure 1). Karyotype analysis of GD2-1260 and iso-GD2-1260 demonstrated no detectable
447 chromosomal abnormalities, confirming the genetic stability of both cell lines (Supplementary
448 Figure 1D). Furthermore, genetic correction did not alter the expression of hiPSC related
449 pluripotent genes (Supplementary Figure 1E). The MLOs derived from WT-75.1, GD2-1260, and
450 iso-GD2-1260 hiPSCs were then compared to evaluating the impact of mutation correction on GD
451 phenotypes.

452

453 At week 8, GCase protein in iso-GD2-1260 MLOs was restored to 45.8% of WT-75.1 levels
454 (Figure 4B, 4C), consistent with correction of one *GBA1* allele [29]. GCase activity also improved,
455 reaching 43.9% and 46.4% of WT-75.1 levels in GD2-1260 hiPSCs and MLOs, respectively,
456 versus approximate 15% in GD2-1260 hiPSCs and MLOs (Figure 4D). Despite reduced GCase,
457 early neural rosette formation in GD2-1260 MLOs remained largely unaffected in GD2-1260 and
458 iso-GD2-1260, with similar counts of SOX2+Ki67+ proliferating neural progenitor cells in neural
459 rosettes (Supplementary Figure 3A, 3B), suggesting early neural development is not impacted by
460 *GBA1* L444P mutation.

461

462 *GBA1* L444P mutation correction ameliorated lipid substrate accumulation in iso-GD2-1260
463 MLOs. GluSph levels which were elevated in GD2-1260 MLOs at weeks 15 and 28
464 (approximately 3.3-fold and 5.6-fold higher than WT-75.1, respectively; $p < 0.01$) was normalized
465 to WT-75.1 levels (Figure 4E). Organoid size of iso-GD2-1260 MLOs was similar to WT-75.1 and
466 GD2-1260 MLOs at week 4, 8 and 15 (Figure 4F, 4G).

467

468 Correction of the L444P mutation restored midbrain and dopaminergic neuron differentiation. TH
469 and FOXA2 levels, which were reduced in week 16 GD2-1260 MLOs by approximately 76.4%
470 and 72.4%, respectively, were restored in iso-GD2-1260 MLOs to WT-75.1 levels for TH, and
471 approximately 53% of WT-75.1 levels for FOXA2 (Figure 4H, 4I). Dopamine levels in iso-GD2-
472 1260 MLOs culture matched those in WT-75.1, unlike the reduced levels in GD2-1260 MLOs
473 (Figure 4J), indicating restored dopaminergic function. The autophagy-lysosomal pathway, which
474 is dysregulated in nGD, was partially corrected by *GBA1* mutation restoration (Figure 4K, 4L).

475 Immunoblot analysis of lysosomal proteins showed that LAMP1 levels, which were significantly
476 decreased in GD2-1260 MLOs by approximately 42.5% versus WT-75.1, were partially restored
477 in iso-GD2-1260 MLOs (Figure 4K, 4L), however, Cathepsin D levels remained unchanged
478 (Figure 4K, 4L). Dysregulated autophagy flux demonstrated by the elevated LC3-II and LC3-I was
479 not significantly improved in isogenic MLOs compared to GD2-1260 MLOs (Figure 4M, 4N).
480
481 GCase deficiency leads to mTOR hyperactivation in nGD [13,54,55]. In GD2-1260 MLOs, levels of
482 4E-BP1 and its phosphorylated form P-4E-BP1 (Thr37/46) were significantly elevated (Figure 4O).
483 These levels were normalized or significantly reduced in iso-GD2-1260 MLOs. While S6 and its
484 phosphorylated form (P-Ser235/236) remain unchanged (Figure 4O, 4P).
485
486 These results demonstrate that CRISPR/Cas9-mediated correction of *GBA1* mutation in GD2-1260
487 hiPSCs effectively rescues key nGD phenotypes and downstream effects, highlighting gene
488 correction as a therapeutic strategy and validating MLOs as a preclinical disease model.
489
490 **SapC-DOPS nanoparticle-mediated GCase enzyme therapy corrects GD phenotypes in GD**
491 **MLOs**
492 SapC-DOPS nanoparticles, composed of saposin C (SapC) and dioleoylphosphatidylserine
493 (DOPS), showed promise as a CNS-targeted delivery system for lysosomal disorders like nGD
494 [38,39]. The effectiveness of this approach in rescuing GD phenotypes was evaluated in MLOs derived
495 from GD2-1260 hiPSCs and another GD2 hiPSC line, GD2-10-257, which carries the
496 *GBA1*$^{L444P/RecNcil}$ mutation [56]. MLOs were derived from these hiPSCs following the protocol in
497 Figure 1 and described in the Methods section. SapC-DOPS nanoparticle was formulated with a

498 fGCase, a recombinant GCase variant with over 21-fold longer active half-life at lysosomal pH
499 than wild-type GCase [57,58] (Figure 5A).
500
501 To test SapC-DOPS uptake, WT-75.1 MLOs were co-cultured with CVM (CellVue Maroon)
502 loaded SapC-DOPS nanoparticles for 48 hours. CVM signals were detected throughout the
503 organoids, confirming successful cargo delivery (Figure 5B). SapC-DOPS-fGCase was then
504 prepared with 0.6 μg/mL fGCase [38] and cocultured with MLOs. After 48 hours, treatment
505 significantly increased GCase activity in GD2-1260 MLOs, restoring it to approximately 66.7%
506 of WT-75.1 levels, confirming efficient delivery (Figure 5C).
507
508 To evaluate efficacy, GD2-1260 and GD2-10-257 MLOs were treated for two weeks with SapC-
509 DOPS or SapC-DOPS-fGCase. Confocal imaging confirmed restored GCase expression, with
510 SapC-DOPS-fGCase-treated GD2-1260 and GD2-10-257 MLOs showing increased GCase
511 approaching the level in WT-75.1 MLO (Figure 5D). Additionally, SapC-DOPS-fGCase treatment
512 significantly elevated GCase load in both dopaminergic neurons (TH+) and astrocytes (GFAP+),
513 as shown by colocalization of GCase with TH and GFAP in GD2-1260 and GD2-10-257 MLOs,
514 respectively (Supplementary Figure 4A-D). Consistent with the results obtained with GD2-1260
515 MLOs (Figure 4H), reduction of TH in GD2-10-257 MLOs at weeks 16 and 28 were evident
516 (Supplementary Figure 4E). Corresponding to increased GCase protein, SapC-DOPS-fGCase
517 treatment elevated GCase activity to 2.3-fold of untreated WT-75.1 MLO (Figure 5E). In GD2-
518 1260 MLOs, SapC-DOPS-fGCase fully restored GCase activity to WT levels, while SapC-DOPS
519 alone had no effect (Figure 5F). Similar GCase restoration was observed in the additional patient
520 organoids, GD2-10-257 MLOs, indicating the effectiveness of this approach across different GD

521 MLO models with various *GBA1* mutations (Figure 5G). Importantly, SapC-DOPS-fGCase
522 significantly reduced elevated GluSph levels in GD2-1260 and GD2-10-257 MLOs, matching WT-
523 75.1 levels (Figure 5H, 5I), confirming effective lipid substrate clearance by delivered fGCase.
524
525 Furthermore, we evaluated the impact of SapC-DOPS-fGCase on the autophagy and lysosomal
526 pathway and mTOR signaling. fGCase was found effectively delivered to lysosomal compartments,
527 evidenced by colocalization of LAMP1 and LC3-II in treated GD2-1260 and GD2-10-257 MLOs
528 (Supplementary Figure 5A-D), indicating restoration of GCase in lysosomal and autophagosome
529 compartments. However, analysis of protein levels showed that decreased LAMP1 expression in
530 GD2-1260 MLOs was not altered following SapC-DOPS-fGCase treatment (Figure 5J). The
531 elevated LC3-II levels, an indicator of impaired autophagic flux, were reduced upon treatment,
532 suggesting enhanced autophagic activity (Figure 5J). Moreover, phosphorylated 4E-BP1
533 (Thr37/46), but not total 4E-BP1, was improved in SapC-DOPS-fGCase treated MLOs, reflecting
534 a decrease in mTOR hyperactivation (Figure 5J). We anticipate that a longer duration of
535 SapC-DOPS-fGCase exposure in nGD MLOs may produce a more robust therapeutic effect in
536 rescuing nGD-associated phenotypes, which will be evaluated in future studies.
537
538 In conclusion, the effective restoration of GCase activity and correction of selected molecular and
539 biochemical GD phenotypes highlight both the utility of the MLO platform for studying nGD and
540 the therapeutic potential of this nanoparticle-based approach for treating nGD.
541
542 **AAV-mediated gene transfer in GD MLOs enhances GCase activity and mitigates GD**
543 **phenotypes**

544 AAV-based gene therapies have shown clinical safety and efficacy in neurodegenerative diseases
545 [59,60]. Trials for GD Type 1 (NCT05487599) and Type 2 (NCT04411654) using AAV9 have initiated.
546 While animal models support AAV's effectiveness in GD, its cellular impact on human or patient
547 derived models remains unknown. To investigate the therapeutic effect of AAV gene therapy in
548 human GD organoids, AAV9-GBA1 was injected at dose of 1.8×10^{10} vg per organoid at week 13
549 and evaluated 3 weeks after the injection (Figure 6A). In WT-75.1 MLOs, GCase activity was
550 significantly increased in AAV9-GBA1-treated MLOs compared to untreated controls at week 15
551 (Figure 6B, left panel), suggesting effective transgene expression in normal organoids. AAV9-
552 GBA1 restored GCase activity in GD2-1260 and GD2-10-257 MLOs to 47.8% and 37.7% of WT-
553 75.1 levels, respectively ($p < 0.001$), compared to 6.0% and 8.8% in untreated controls (Figure 6B,
554 middle and right panel). Immunoblot results further confirmed the restoration of GCase protein in
555 AAV9-GBA1 treated GD MLOs (Figure 6B, bottom panel). Mass spectrometry analysis showed
556 that AAV9-GBA1 normalized GluSph levels in GD2-1260 and GD2-10-257 MLOs, contrasting
557 with elevated levels in untreated MLOs versus WT-75.1 controls (Figure 6C), indicating effective
558 clearance of toxic lipid substrates in MLO by AAV gene therapy. Of note, LAMP1 levels were
559 elevated after AAV9-GBA1 treatment, reflecting correction of lysosomal dysfunction (Figure 6D).
560 However, the protein level of DA neuron marker (TH) was not significantly increased after AAV
561 gene therapy compared to untreated group, suggesting longer treatment or earlier gene therapy
562 intervention might be needed to recover dopaminergic neurons. Confocal imaging corroborated
563 that AAV9-GBA1-treated GD2-1260 MLOs exhibited GFP signals and restored GCase expression
564 in pan-neurons, DA neurons and astrocytes (Figure 6E).
565

566 These results collectively demonstrate that AAV9-GBA1 gene therapy effectively corrected GCase
567 deficiency, reduced GluSph accumulation, and ameliorates lysosomal pathology in GD MLOs,
568 highlighting its therapeutic potential for nGD.
569
570 **Substrate Reduction Therapy reduces lipid accumulation and improves lysosomal function**
571 **in GD MLOs**
572 Current Substrate Reduction Therapy (SRT) in the standard clinical treatments for GD [61,62] has
573 limited efficacy in addressing the neurological manifestations of nGD due to their inability to cross
574 the blood-brain barrier efficiently. GZ-682452 (termed herein as GZ452) is an analogue of
575 venglustat that is presently under clinical evaluation for treating nGD [63]. To evaluate the human
576 MLO as a preclinical model for SRT drug development, we assessed GZ452's effects on MLO
577 growth, lipid accumulation, midbrain markers, and lysosomal function.
578
579 GZ452 toxicity was first evaluated in WT-75.1 MLOs. Treatment at 0.3, 1, 2, 3 μM over 6 weeks
580 modestly reduced MLO size at 1 μM, with the 2 μM and 3 μM doses significantly decreasing size
581 versus untreated controls (Figure 7A), indicating high dose of GZ452 notably suppressed MLO
582 growth. We next tested GZ452 at doses (0.01, 0.05, 0.3 μM) over 6 weeks in WT-75.1 MLOs.
583 GZ452 dose-dependently reduced total GluCer levels (Figure 7B) and GluCer species, with the
584 0.3 μM dose showing the most pronounced effect (Figure 7C).
585
586 Expression of midbrain markers *ASCL1*, *TH*, and *PLZF* in WT-75.1 MLOs was largely unaffected
587 by GZ452 (0.3 μM) treatment started at week 6, with no significant changes in relative mRNA
588 levels compared to untreated controls (Supplementary Figure 6). We therefore applied this optimal

589 tolerated GZ452 dose of 0.3 μM (300nM) in short-term (2 weeks) and long-term (up to 28 weeks)
590 treatment to test its therapeutic effects in GD MLOs. After two weeks of treatment starting in week
591 13, GZ452 significantly ameliorated GluCer and GluSph accumulation in GD2-1260 MLOs
592 (Figure 7E, 7F). Long-term GZ452 treatment from day 2 to week 28 robustly cleared GluSph
593 storage and normalized it to the WT level (Figure 7G, 7H). Immunoblot analysis showed that long-
594 term GZ452 treatment improved lysosomal function, partially restoring LAMP1 levels (0.8 ± 0.1;
595 $p < 0.05$) and reducing LC3-II by 21.4% ($p < 0.01$) (Figure 7I, 7J). These findings demonstrate
596 that GZ452 effectively reduced lipid accumulation and improves lysosomal function in GD MLOs,
597 supporting its therapeutic potential for ameliorating key disease phenotypes.
598

599 **Discussion**

600 We developed MLOs from two GD Type 2 patient-derived hiPSCs, offering deepened
601 understanding to disease pathogenesis and an advanced model system for drug discovery. To our
602 knowledge, this is the first GD brain organoid model derived from patient cells. These GD MLOs
603 harbor prevalent *GBA1*$^{L444P/P415R}$ and *GBA1*$^{L444P/RecNcil}$ mutations, replicated key nGD phenotypes,
604 including reduced GCase activity, glycosphingolipids accumulation, lysosomal abnormalities, and
605 impaired dopaminergic neuron differentiation (Supplementary Table 2). Emerging interventions,
606 CRISPR/Cas9-mediated gene correction, SapC-DOPS-fGCase nanoparticle, and AAV9-GBA1
607 gene therapy, significantly restored GCase function and mitigate disease hallmarks in GD MLOs,
608 supporting their use in preclinical studies (Supplementary Table 2). Additionally, dysregulated Wnt
609 signaling and impaired dopaminergic neuron differentiation in GD MLOs provides novel insights
610 into nGD pathogenesis and potential therapeutic targets. This research underscores the utility of
611 patient-derived MLOs as a human-relevant platform for modeling disease complexity and testing
612 drug responses to bridge preclinical and clinical research.

613

614 Our findings revealed nGD-specific phenotypes in MLOs, including reduced GCase activity,
615 GluCer and GluSph accumulation, and altered mTOR and autophagosome-lysosomal pathways,
616 closely reflecting patient neuropathology [4,55]. Unlike *Gba1* knockout animal models, which lack
617 patient-specific genetic and epigenetic diversity, patient-derived MLOs retain heterozygous or
618 compound heterozygous background, enabling study of disease mechanisms and modifier genes.
619 Partial rescue in isogenic iso-GD2-1260 MLOs, where mutation correction alleviated but did not
620 fully resolve abnormalities, highlights the model's value in capturing nGD pathology and guiding
621 personalized precision therapeutic strategies. This model offers a more advanced and

622 physiologically relevant platform than traditional gene knockout or transgenic models, better
623 capturing the complexity of nGD pathology.
624
625 Transcriptomic analysis of GD MLOs uncovered dysregulated Wnt signaling, a critical pathway
626 in early brain development, highlighting a mechanistic insight into nGD pathogenesis. Aligning
627 with Awad et al., who reported that downregulated Wnt/β-catenin signaling impairs DA neuron
628 differentiation in nGD hiPSC-derived neuronal progenitors [30], our MLOs exhibited reduced
629 FOXA2+ DA progenitors and TH+ mature DA neurons, along with decreased dopamine release in
630 culture medium. Transcriptome analysis of the GD MLOs identified 1,429 differentially expressed
631 genes enriched in Wnt signaling, axon guidance and neuron differentiation pathways, indicating
632 that GCase deficiency disrupts midbrain patterning and neuronal specification. This finding is
633 further supported by reduced expression of midbrain markers (e.g., FOXA2, TH), reduced
634 dopamine release from DA neurons, and skewed forebrain/midbrain patterning genes (e.g., FOXP1,
635 FOXG1) in GD MLOs. Compared to *GBA1* KO iPSC-derived midbrain-like organoids, which
636 showed only a marginal reduction in dopaminergic neuron differentiation and no significant
637 dysregulation of FOXG1 expression [24], our MLO model exhibits a distinct and more disease-
638 relevant phenotype. These results suggest that aberrant Wnt signaling contributes to impaired
639 dopaminergic neuron development and may drive the disease pathogenesis in nGD. Thus, targeting
640 Wnt-related pathways could offer a therapeutic strategy to address early developmental defects in
641 nGD. Comparative analysis with prior transcriptomic data from nGD mouse midbrain showed
642 consistent dysregulation in axon guidance, synaptic signaling, lipid metabolism, and nervous
643 system development etc. (Supplementary Table 3) [13], supporting the fidelity of our human MLO
644 model. Moreover, midbrain organoids at 35 days of development closely correspond to the human

645 embryonic midbrain at approximately 9 weeks, while 70-day-old organoids align more closely
646 with the 10-week stage [64]. These correlations highlight the importance of initiating treatment
647 during the fetal stage, which may be critical for preventing the disease.
648
649 Isogenic MLOs generated by correcting the *GBA1* L444P mutation in GD2-1260 hiPSCs using
650 CRISPR/Cas9 revealed the key genetic mechanisms in nGD. The resulting WT/P415R genotype
651 in iso-GD2-1260 partially rescued nGD phenotypes. GCase activity restored to nearly 50% of WT-
652 75.1 levels, with normalized GluSph levels and improved TH expression. However, partial
653 recovery of FOXA2 (53% of WT-75.1), along with persistent LC3 and LAMP1 abnormalities, may
654 contribute to remaining pathology. These findings imply that the retained P415R mutation in this
655 isogenic line may contribute to residual lysosomal dysfunction, potentially exerting a negative
656 effect, as it has been reported to be associated with altered GCase stability and activity in previous
657 studies [65,66]. The partial rescue in iso-GD2-1260 MLOs suggests that the P415R mutation may
658 affect disease severity and therapeutic response, deserving further investigation into the specific
659 role of P415R mutation in GD and assessing whether dual mutation correction is required for full
660 phenotypic normalization.
661
662 Evaluation of GZ452, a CNS-accessible SRT drug [67], in GD2-1260 MLOs showed significant
663 reduction in GluCer and GluSph levels at a well-tolerated dose, alongside partial restoration of
664 lysosomal and autophagy markers (LAMP1, LC3-II). Unlike higher doses that affected organoid
665 growth, 0.3 μM preserved MLO size and expression of midbrain markers (ASCL1, TH, PLZF)
666 involved in organoid differentiation and growth. These findings underscore the value of the MLOs
667 for assessing drug safety (e.g., organoid size as toxicity indicator) and efficacy in a human-specific,

668 midbrain-relevant model before clinical studies. Our study demonstrated positive therapeutic
669 outcomes using AAV9-GBA1 gene therapy and SapC-DOPS nanoparticle-mediated GCase
670 delivery in GD2-1260 and GD2-10-257 MLOs. AAV9-GBA1 restored GCase activity, while
671 SapC-DOPS-fGCase elevated GCase activity to WT levels, both approaches effectively reduced
672 GluSph. Based on prior studies showing no region-specific effects in GD patients and mice, these
673 therapies may also be effective in other brain organoid types, such as COs [4,41]. The novelty of
674 employing MLOs lies in their ability to concurrently test these diverse therapeutic modalities: SRT,
675 gene therapy, and nanoparticle-based enzyme delivery within a patient-derived system that
676 replicates nGD pathology, offering the unique patient-MLO system to assess complex cellular
677 responses that directly reflect patient specific conditions.
678
679 Unlike animal models, MLOs provide a controlled environment to evaluate dose-dependent effects
680 and cellular responses, enabling the identification of optimal therapeutic windows while
681 minimizing the risk of adverse outcomes in patients with nGD. Moreover, FDA has increasingly
682 encouraged the use of organoid systems in drug development, recognizing their potential to
683 improve preclinical testing and reduce reliance on animal models. Therefore, the adaptability of
684 MLOs to test advanced interventions, coupled with their alignment with regulatory trends favoring
685 human-relevant models, positions them as a great tool for accelerating the translation of innovative
686 treatments from preclinical research to clinical application.
687
688 There are limitations in our current MLOs, such as lacking vascular system and microglia. The
689 absence of microglia and vasculature may contribute to incomplete phenotyping and phenotypic
690 rescue observed in our therapeutic experiments. Without vascularization, cells in the core may

experience hypoxic and nutrient deprivation, leading cell death or necrosis in deeper layers in long-term culture. This limitation may partially explain the incomplete restoration of dopaminergic markers (TH, FOXA2) and partial recovery of LAMP1 following SapC-DOPS-fGCase and AAV9-GBA1 treatments. Additionally, the lack of microglia limits molding of neuroinflammatory, which contributes to the clearance of toxic lipid substrates and mediating neuronal damage in GD. Elevated GluSph and impaired dopaminergic differentiation observed in GD MLOs may not fully reflect inflammatory process. Dysregulated Wnt signaling and lysosomal and autophagic markers (LAMP1, LC3-II/I) could be amplified by microglial activation *in vivo*. To improve model fidelity, future studies would incorporate vascularization (e.g., endothelial co-culture or microfluidics) to enhance oxygen and nutrient distribution and integrate microglia via directed differentiation [68] or co-culture with hiPSC-derived microglia [69] to enhance the relevance of MLOs for long-term nGD research and drug testing.

In conclusion, patient-derived MLOs offer an advanced, human-relevant platform for elucidating nGD pathogenesis and evaluating therapies, overcoming limitations of traditional models. Dysregulated Wnt signaling and impaired dopaminergic neuron differentiation, along with partial rescue of phenotypes through gene correction, highlight the complex genetic and developmental underpinnings of nGD. The efficacy assessment of SapC-DOPS-fGCase, AAV9-GBA1 and SRT-GZ452 therapies underscores the targeted interventions and safety evaluation of these approaches in patient-derived brain organoid models. While limitations such as lack of vascularization and microglia constrain modeling of neuroinflammation, these challenges can be addressed as discussed above and using advanced culturing techniques. Collectively, our findings lay the groundwork for developing patient-specific preclinical models to support personalized therapeutic

714 strategies, while also advocating for the continued refinement of MLO systems to accelerate the

715 discovery of effective treatments for nGD.

716

717 **Acknowledgments**

718 This work was supported by the Cincinnati Children's Pluripotent Stem Cell Facility (RRID:
719 SCR_022634), Clinical and Biomedical Mass Spectrometry Facility (RRID: SCR_022638) and
720 Transgenic Animal and Genome Editing Facility (RRID: SCR_022642). Authors acknowledge
721 Freeline Therapeutics (now Spur Therapeutics) for providing the fGCase under a Material Transfer
722 Agreement.

723

724 **Additional information**

725 **Funding**

726 This work is supported by awards from the National Institute of Health (grant number
727 R21HD1027881, R21OD033660 and R01NS138309 to Y.S.; R01NS103931 partly to Y.S.;
728 R21HD1027881 partly to C.N.M.; R01NS138309 partly to X.Q.); the National Center for
729 Advancing Translational Sciences of the National Institutes of Health (Award Number
730 2UL1TR001425-05A1, CHMC-CTSA 00003827 to Y.S.); Cincinnati Children's Hospital Medical
731 Center (CCHMC) Center of Pediatric Genomics Award to Y.S.; CCHMC Research Innovation
732 Pilot Funding Program Award to Y.S., Y.L. and J.E.H. The funding source did not have any role in
733 study design, data collection, data analyses, interpretation, or writing of report.

734

735 **Author Contributions**

736 Y.L. designed experiments, cultured hiPSCs and MLOs, performed experiments, analyzed data,
737 and wrote the manuscript. B.L. measured GCase enzyme activity in hiPSCs and MLOs. V.F.
738 carried out lipid extract from hiPSCs and MLOs, W.Z., X.Z., R.L.B. and K.DR.S performed
739 quantification of GluCer/GluSph by LC-MS/MS and data analysis. S.A. assisted with

740 immunofluorescence staining and immunoblot assays. C.N.M and YC.H made isogenic hiPSC
741 cells and conceived experimental designs and edited the manuscript. J.T. conceived experimental
742 designs and edited the manuscript. J.E.H. generated cerebral organoid and edited manuscript. A.K.
743 and X.Q. provided SapC-DOPS nanoparticles and guidance for the enzyme uptake assay. R.A.F
744 provided an nGD hiPSC cell line and edited the manuscript. Y.S. conceived experimental designs,
745 supervised the project, wrote the manuscript, and provided funding to the study.
746

747 **Ethics**

748 This work has been reviewed and approved by the Cincinnati Children's Hospital Medical Center
749 (CCHMC) and University of Cincinnati (UC) Embryonic Stem Cell Research Oversight (ESCRO)
750 committee under ESCRO protocol #EIPHG3114_R3. Primary fibroblast (GM01260) for
751 generating GD2-1260 iPSC was obtained from the Coriell Institute for Medical Research under
752 Material Transfer Agreement. WT-75.1 iPSC was generated using fibroblasts cultured from
753 discarded circumcision tissue obtained from a healthy donor (provided by Dr. Susanne Wells,
754 Division of Hematology/Oncology, CCHMC; institutional review board no. 02-9-29X) at CCHMC.
755 The procedures used to generate the GD2-1260 iPSC and WT-75.1 iPSC lines at CCHMC have
756 been reviewed and approved by CCHMC/UC ESCRO committee. Skin biopsies to generate GD2-
757 10-257 iPSCs were obtained from NIH with informed consent and were approved by the
758 Institutional Review Board (IRB). The procedures used to generate the GD-2-10-257 nGD iPSC
759 line at the University of Maryland Baltimore (UMB) have been reviewed and approved by the
760 UMB IRB and ESCRO committees.
761

762 **Conflict of Interests**

763 K.D.R.S. discloses outside this work equity in Asklepion Pharmaceuticals, Baltimore, and Aliveris
764 s.r.l. Italy and is a consultant to Mirum Pharmaceuticals. Other authors declare no competing
765 interests.
766

767 **Figures**

Fig. 1

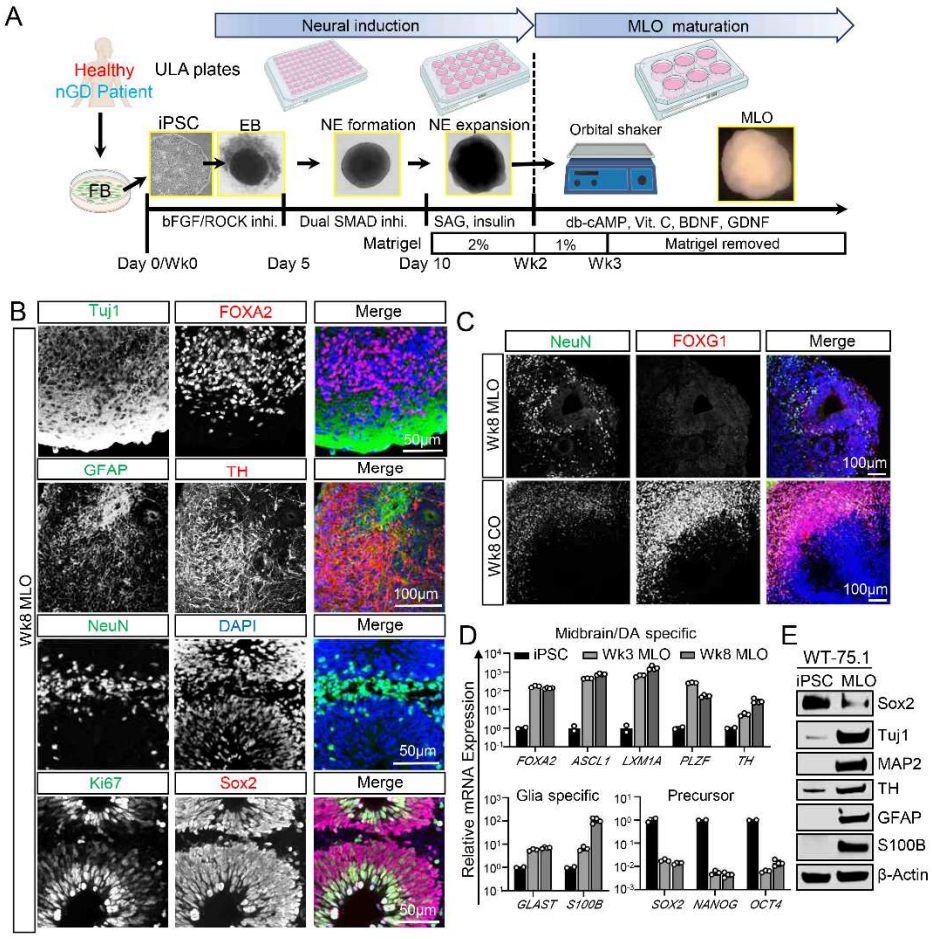

768 **Figure 1. Generation and characterization of midbrain-like organoids (MLOs) from healthy**

769 **human (h) iPSCs (WT-75.1 hiPSCs)**.

770 (A) A schematic overview of the procedures for generating MLOs from healthy WT-75.1 hiPSCs.

771 (B) Representative confocal images showing architectural structure of week (Wk) 8 MLOs

772 containing new-born neurons (Tuj1/NeuN), astrocytes (GFAP), dopaminergic neurons

773 (FOXA2/TH) and neural progenitor cells (SOX2/Ki67). Merge images show the distribution of

774 those cell markers.

775 (C) FOXG1 expression in MLO and cerebral organoid (CO). Transcription factor FOXG1
776 (forebrain marker) was enriched in CO at Wk8 of differentiation but absent in MLO. Pan-neurons
777 (NeuN) were both present in MLO and CO, as shown by NeuN immunostaining (neuronal marker).
778 (D) Quantitative analysis of cell type specific genes expression for midbrain/dopaminergic neuron
779 (*FOXA2*/*ASCL1*/*LXM1A*/*PLZF*/*TH*), glial cells (*GLAST*/*S100B*) and multipotent stem cells
780 (*SOX2*/*NANOG*/*OCT4*) in Wk3 and Wk8 MLOs (n=3 MLOs pooled for each group) by qRT-PCR.
781 (E) Immunoblot of Sox2, Tuj1, MAP2, TH, GFAP and S100B in WT-75.1 hiPSCs and its derived
782 MLO (Wk8, n=3 MLOs pooled for each group) lysate. β-Actin was used as a loading control.

Fig. 2

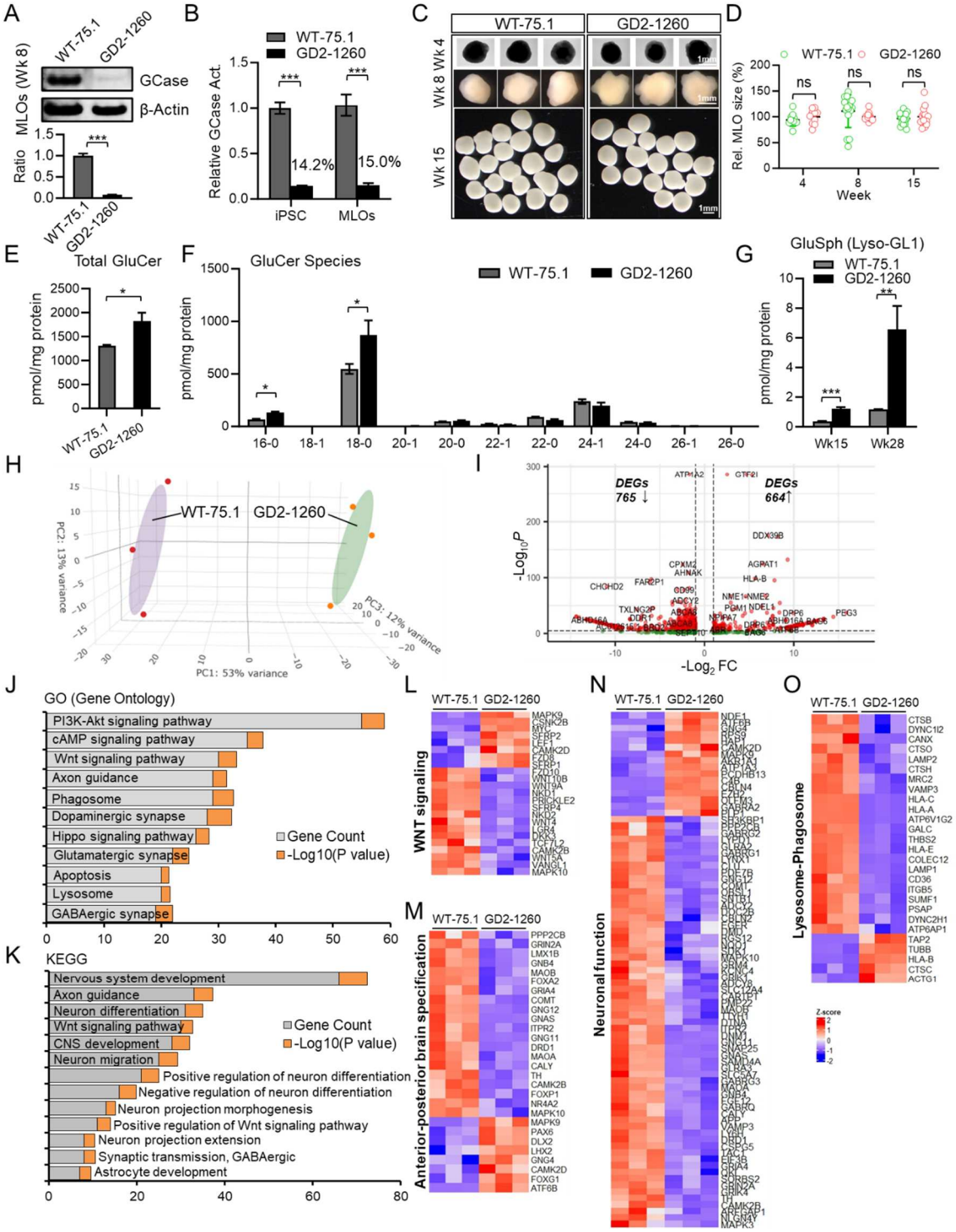
A
WT-75.1
GD2-1260
MLOs (Wk 8)
GCase
β-Actin
Ratio
B
WT-75.1
GD2-1260
Relative GCase Act.
14.2%
15.0%
iPSC
MLOs
C
WT-75.1
GD2-1260
Wk 8
Wk 4
Wk 15
D
WT-75.1
GD2-1260
Rel. MLO size (%)
ns
Week
E
Total GluCer
pmol/mg protein
F
GluCer Species
pmol/mg protein
16-0
18-1
18-0
20-1
20-0
22-1
22-0
24-1
24-0
26-1
26-0
G
GluSph (Lyso-GL1)
pmol/mg protein
Wk15
Wk28
H
WT-75.1
GD2-1260
PC1: 53% variance
PC2: 13% variance
PC3: 12% variance
I
DEGs 765 ↓
DEGs 664↑
-Log10P
-Log2 FC
J
GO (Gene Ontology)
PI3K-Akt signaling pathway
cAMP signaling pathway
Wnt signaling pathway
Axon guidance
Phagosome
Dopaminergic synapse
Hippo signaling pathway
Glutamatergic synapse
Apoptosis
Lysosome
GABAergic synapse
Gene Count
-Log10(P value)
K
KEGG
Nervous system development
Axon guidance
Neuron differentiation
Wnt signaling pathway
CNS development
Neuron migration
Positive regulation of neuron differentiation
Negative regulation of neuron differentiation
Neuron projection morphogenesis
Positive regulation of Wnt signaling pathway
Neuron projection extension
Synaptic transmission, GABAergic
Astrocyte development
Gene Count
-Log10(P value)
L
WT-75.1
GD2-1260
WNT signaling
M
WT-75.1
GD2-1260
Anterior-posterior brain specification
N
WT-75.1
GD2-1260
Neuronal function
O
WT-75.1
GD2-1260
Lysosome-Phagosome
Z-score

783

784

785 **Figure 2. GCase deficiency drives glycosphingolipids accumulation and transcriptomic**
786 **alteration in GD MLOs.**
787 The GD MLOs were generated as in Figure 1A.
788 (A) Reduced GCase protein in GD MLO (GD2-1260). Wk 8 MLOs (n=3) were pooled as a
789 biological sample. β-Actin was used as loading control.
790 (B) GCase activity in hiPSCs and MLOs (> 3 MLOs were pooled for each group). Data was
791 normalized to WT-75.1 control.
792 (C) Representative images of WT-75.1 and GD2-1260 MLOs at Wks 4, 8 and 15 of differentiation.
793 (D) MLO size was measured based on area of MLO spheres and normalized to WT-75.1 control
794 at each indicated time points. N ≥ 10 MLOs were quantified per group.
795 (E, F) Measurement of total glucosylceramide (GluCer) and GluCer species in Wk 15 MLO.
796 (B, D, E. G) *$p < 0.05$, ***$p < 0.001$, ns, not significant, unpaired Student's t test.
797 (G) Glucosylsphingosine (GluSph) levels in Wk15 and Wk28 MLOs (3~5 MLOs were pooled for
798 each group). GluCer and GluSph levels in the organoids were measured by LC-MS/MS and
799 normalized by corresponding total protein of MLO tissue lysate.
800 (H) 3D Principal Component Analysis (PCA) of bulk RNA sequencing (RNA-seq) data. The
801 Euclidean distance of the normalized gene expression among healthy control (WT-75.1) and GD
802 (GD2-1260) MLOs was used for sample clustering. Ellipsoids around each group indicate the
803 distribution and spread of the samples within the sample group. Wk 8 MLOs (n=3) were pooled
804 as one biological sample, and three samples were profiled in each group.
805 (I) MA plot showing the distinct genes differentially expressed in GD MLOs. Statistically
806 significant differentially expressed genes (DEGs; |fold change|≥ 1, p-adj ≤ 0.05 and base mean ≥

807 50) were highlighted in red. Number of DEGs downregulated and upregulated in GD2-1260 MLO
808 against WT-75.1 MLO were shown. FC, fold-change.
809 (J, K) Dysregulated pathway in GD MLOs analyzed by GO (gene ontology) (J) and Kyoto
810 Encyclopedia of Genes and Genomes (KEGG) (K) enrichment of DEGs. Both gene counts and
811 level of significance (-log10 of *p* value) were shown as stacked columns for each category.
812 (L-O) Heat maps of dysregulated pathways or biological functions in GD MLO. Specifically,
813 aberrant expressions of genes involved in WNT signaling (L), anterior-posterior brain specification
814 (M), neuronal function (N) and lysosome-phagosome (O) were shown.
815

Fig. 3

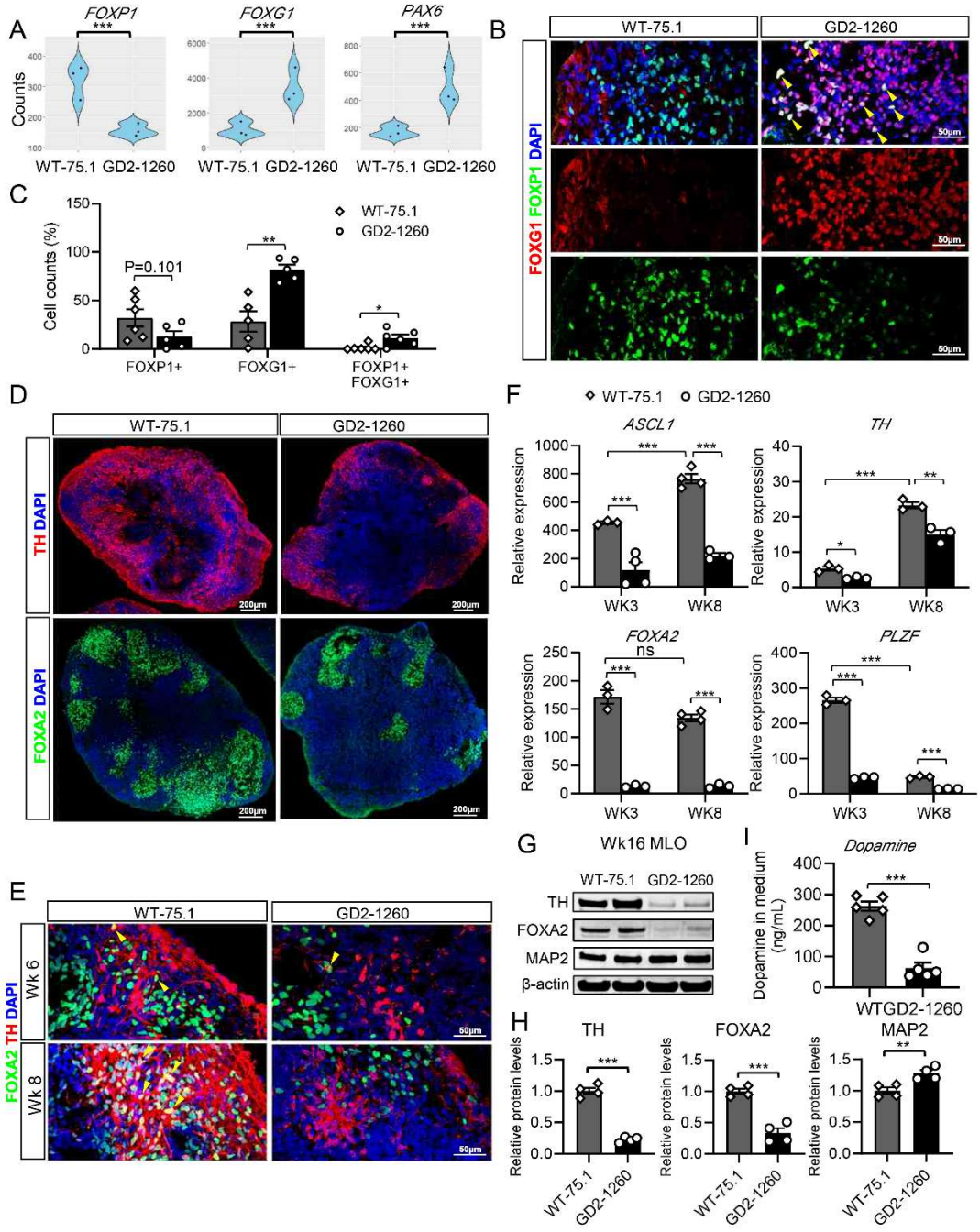

816 **Figure 3. Skewed specification of midbrain patterning and dopaminergic neuron**

817 **differentiation in GD MLOs**.

818 (A) Gene expression of *FOXP1*, *FOXG1*, and *PAX6* in week 8 WT-75.1 and GD2-1260 MLOs.
819 Data were plotted using RNA sequencing counts. ***$p < 0.001$, unpaired Student's t test.
820 (B, C) Aberrant expression of FOXP1/FOXG1 transcription machinery for forebrain/midbrain
821 patterning in GD MLOs. Representative confocal images (B) and quantification of Wk8 WT-75.1
822 and GD2-1260 MLOs, immunostained for FOXP1 (red) and FOXG1 (green), with DAPI (blue)
823 labeling nuclei. Yellow arrows indicate FOXP1+FOXG1+ cells. Scale bar, 50 µm. *$p < 0.05$, **p
824 < 0.01, unpaired Student's t test.
825 (D) Confocal images of Wk6 MLOs, immunostained for midbrain patterning markers FOXA2
826 (green) or TH (red), with DAPI (blue) labeling nuclei. Scale bar, 100 µm.
827 (E) Representative images of differentiating DA neurons in MLOs derived from WT-75.1 and
828 GD2-1260 hiPSCs. TH (red), FOXA2 (green) were co-stained, with DAPI (blue) labeling nuclei.
829 Yellow arrows indicate TH+FOXA2+ cells. Scale bar, 50 µm.
830 (F) Quantification of midbrain progenitor markers *ASCL1*, *TH*, *LMX1A*, and *PLZF* expression in
831 WT-75.1 and GD2-1260 MLOs at Wk3 and Wk8, measured by qRT-PCR and normalized to WT-
832 75.1 hiPSC cells. Data are presented as mean ± SEM (n = 3-4 MLOs per group). *$p < 0.05$, **$p <$
833 0.01.
834 (G) Immunoblot analysis of midbrain/dopaminergic neuron markers TH, FOXA2, and MAP2 in
835 Wk16 MLOs. Protein samples were extracted from n=3 MLOs from each group. β-Actin was used
836 as a loading control.
837 (H) Relative protein levels of TH, FOXA2, and MAP2 in Wk8 GD2-1260 MLOs compared to
838 WT-75.1. *$p < 0.05$, **$p < 0.01$, unpaired Student's t test.

839 (I) Dopamine levels in MLO culture medium assay by ELISA. Culture medium from 4 GD2-1260

840 MLOs or WT-75.1 MLOs at Wk12 cultured in 3 mL BGM medium for 72 hours was assayed. Data

841 are presented as mean ± SEM (n = 5 per group). ***$p < 0.001$, unpaired Student's t test.

842

Fig. 4

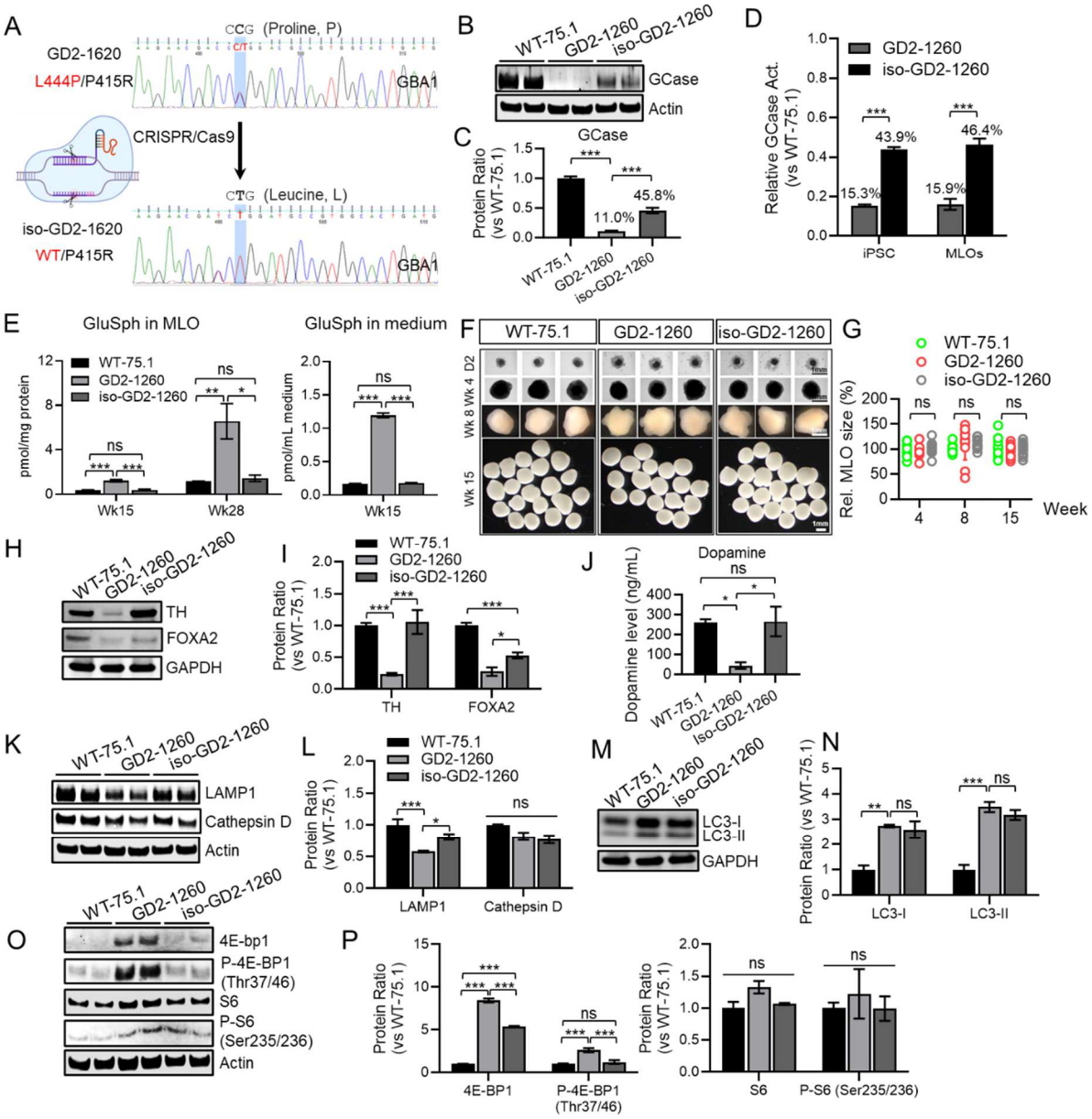

Figure 4. Mutation correction significantly rescued disease phenotypes in GD MLOs.

(A) Schematic overview of CRISPR/Cas9-mediated mutation correction of the *GBA1* L444P mutation in GD2-1260 hiPSCs, converting the L444P (L444P/P415R) mutation (Proline, P to Leucine, L) to the wild-type sequence (WT-P415R), generating isogenic iso-GD2-1260 hiPSCs.

848 The mutated base C in amino acid code 'CCG' for proline (P), was corrected to T to decode leucine
849 (L, CTG), which was confirmed by genome sequencing of *GBA1* locus.
850 (B, C) Immunoblot analysis of GCase protein and quantification in week 8 MLOs derived from
851 WT-75.1, GD2-1260, and iso-GD2-1260 hiPSCs. β-Actin was used as a loading control. Data are
852 presented as mean ± SEM (n = 2 pooled, and 3 biological replicates per group). ***$p < 0.001$.
853 (D) Relative GCase activity in GD2-1260 and iso-GD2-1260 hiPSCs and Wk8 MLOs, normalized
854 to WT-75.1 controls. Data are presented as mean ± SEM (2 MLOs pooled, n = 3 per group). ***p
855 < 0.001.
856 (E) Measurement of GluSph levels in WT-75.1, GD2-1260, and iso-GD2-1260 MLOs at Wk15
857 and Wk28 and their culture medium at Wk 15, quantified by LC-MS/MS and normalized to total
858 protein of tissue lysate. Data are presented as mean ± SEM. For GluSph in MLO, three MLOs
859 were pooled and n = 3 per group. For MLO secreted GluSph, MLO culture medium in wells
860 containing four MLOs were collected, n = 3 per group. **$p < 0.01$; ns, not significant.
861 (F) Representative bright-field images of WT-75.1, GD2-1260 and iso-GD2-1260 MLOs at Day 2,
862 Wks 4, 8, and 15 of differentiation. Scale bar, 1 mm. For side-by-side comparison, images for WT-
863 75.1 and GD2-1260 at Wks 4, 8 and 15 were taken from Fig 2C.
864 (G) MLO size quantification for WT-75.1, GD2-1260 and iso-GD2-1260 MLOs at Wks 4, 8, and
865 15. MLOs size was analyzed by NIS elements and presented as the area (μm^2) of MLO at indicated
866 time point. N ≥ 10 MLOs were quantified per group. Data are presented as mean ± SEM. One-
867 Way ANOVA, ns, not significant.
868 (H, I) Immunoblot analysis of midbrain/dopaminergic neuron markers TH and FOXA2 (H) and
869 their relative quantification (I) in Wk8 MLOs. Protein samples were extracted from n=3 MLOs
870 from each group. GAPDH was used as a loading control.

871 (J) Dopamine levels in the culture medium of Wk12 MLOs derived from WT-75.1, GD2-1260 and
872 iso-GD2-1260 hiPSCs, measured after 72 hours in BGM medium (n = 4 MLOs per samples, 3
873 biological replicates). Data are presented as mean ± SEM (n = 5 per group). *$p < 0.05$, unpaired
874 Student's t test.
875 (K, L) Immunoblot analysis of autophagy-lysosomal pathway markers LAMP1 and Cathepsin D
876 (K) and quantification (L) in Wk16 MLOs. GAPDH was used as a loading control. Data are
877 presented as mean ± SEM.
878 (M, N) Immunoblot analysis of LC3-I and LC3-II (M) and quantification (N) in Wk16 MLOs.
879 Protein samples were extracted from n=3 MLOs for each group. GAPDH was used as a loading
880 control.
881 (O) Immunoblot analysis of mTOR signaling pathway components [4E-BP1, P-4E-
882 BP1(THR37/46), S6, and P-S6 (Ser235/236)] in Wk16 MLOs. β-Actin was used as a loading
883 control.
884 (P) Quantification of protein levels of mTOR signaling pathway components. Data are normalized
885 to WT-75.1 and presented as mean ± SEM.
886 Immunoblot analysis for panel H and I and K-P was performed using the lysate from 3 MLOs
887 pooled per group, 3 repeated experiments. ***$p < 0.001$; ns, not significant. One-way ANOVA test
888 with Tukey's test.
889
890

Fig. 5

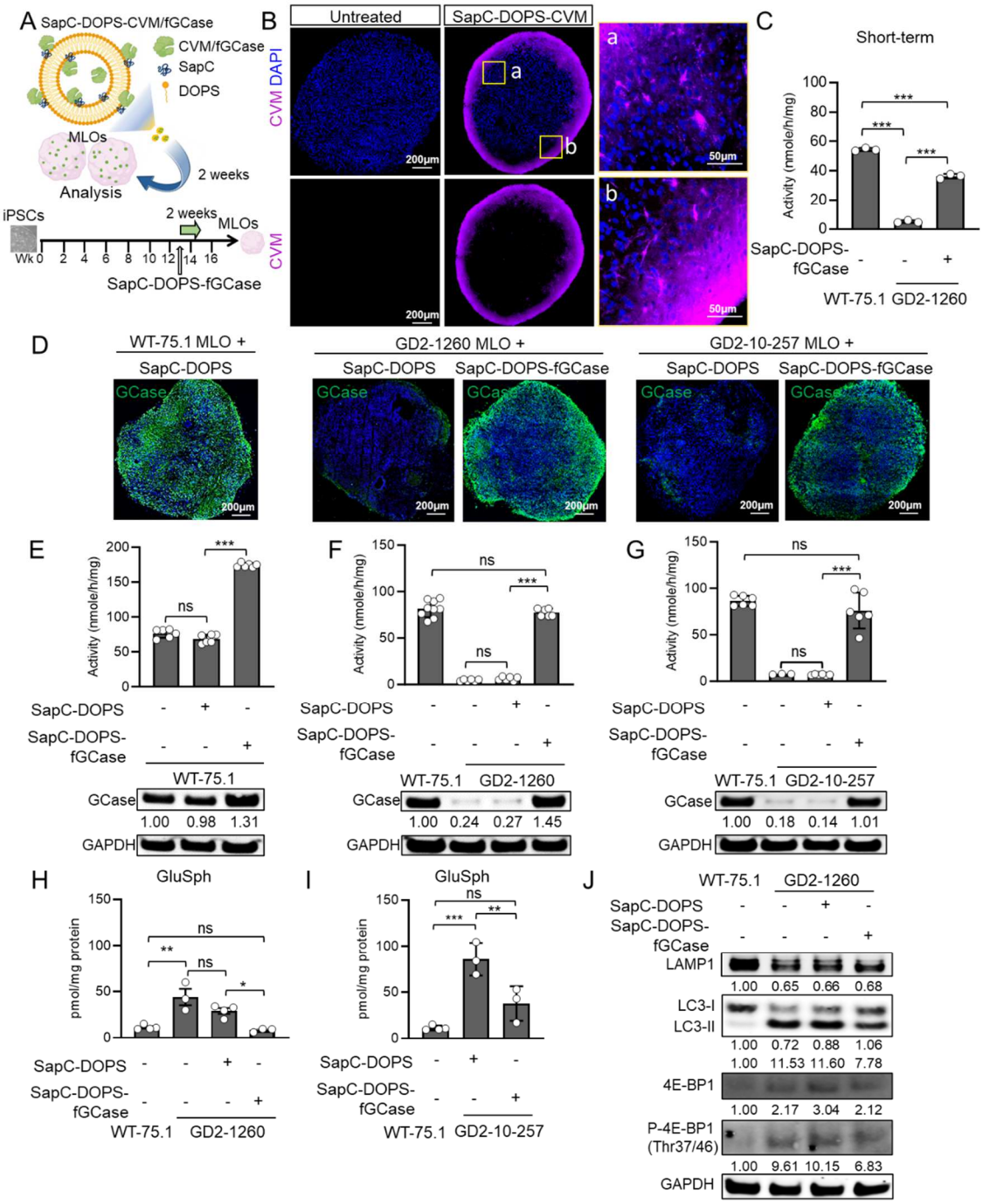

Figure 5. Delivery of GCase to MLOs via SapC-DOPS nanoparticles corrects GD phenotypes. (A) Schematic illustration of SapC-DOPS nanoparticle-mediated delivery of recombinant GCase (fGCase) to MLOs. SapC-DOPS nanoparticles carrying fGCase or fluorescent label CVM were

894 cocultured with MLOs, followed by short-term (48 hours) or 2-week treatment period before
895 analysis.
896 (B) Confocal images of untreated and SapC-DOPS-CVM-treated MLOs, showing uptake of CVM
897 (magenta) with DAPI (blue) labeling nuclei. Scale bars: 200 µm (left panel), 50 µm (right panels,
898 magnified regions a and b).
899 (C) GCase activity in WT-75.1 and GD2-1260 MLOs following a 48-hour treatment with SapC-
900 DOPS-fGCase. Data are presented as mean ± SEM (3 MLOs pooled, n = 3 per group). ***p <
901 0.001.
902 (D) Confocal images of WT-75.1, GD2-1260, and GD2-10-257 MLOs treated with SapC-DOPS
903 or SapC-DOPS-fGCase for 2 weeks, immunostained for GCase (green) with DAPI (blue) labeling
904 nuclei. Scale bar, 200 µm.
905 (E-G) GCase activity and protein in WT-75.1 and GD (GD2-1260, GD2-10-257) MLOs treated
906 with SapC-DOPS or SapC-DOPS-fGCase for 2 weeks, measured by enzymatic assay and
907 immunoblot. Data are presented as mean ± SEM (3 MLOs pooled, n = 3~4 per group). ***p <
908 0.001; ns, not significant. Protein samples were extracted from n=3 MLOs for each group.
909 (H, I) GluSph levels in WT-75.1 and GD (GD2-1260, GD2-10-257) MLOs treated with SapC-
910 DOPS or SapC-DOPS-fGCase for 2 weeks, quantified by LC-MS/MS and normalized to total
911 protein. Data are presented as mean ± SEM (3 MLOs pooled, n = 3-4 per group). ***p < 0.001;
912 **p < 0.01; ns, not significant.
913 (J) Immunoblot analysis of autophagy-lysosomal and mTOR pathway proteins in SapC-DOPS or
914 SapC-DOPS-fGCase treated GD2-1260 MLOs. GAPDH was used as a loading control. Protein
915 samples were extracted from n=3 MLOs for each group. Protein levels are normalized to WT-
916 75.1 untreated controls (set to 1.0).

Fig. 6

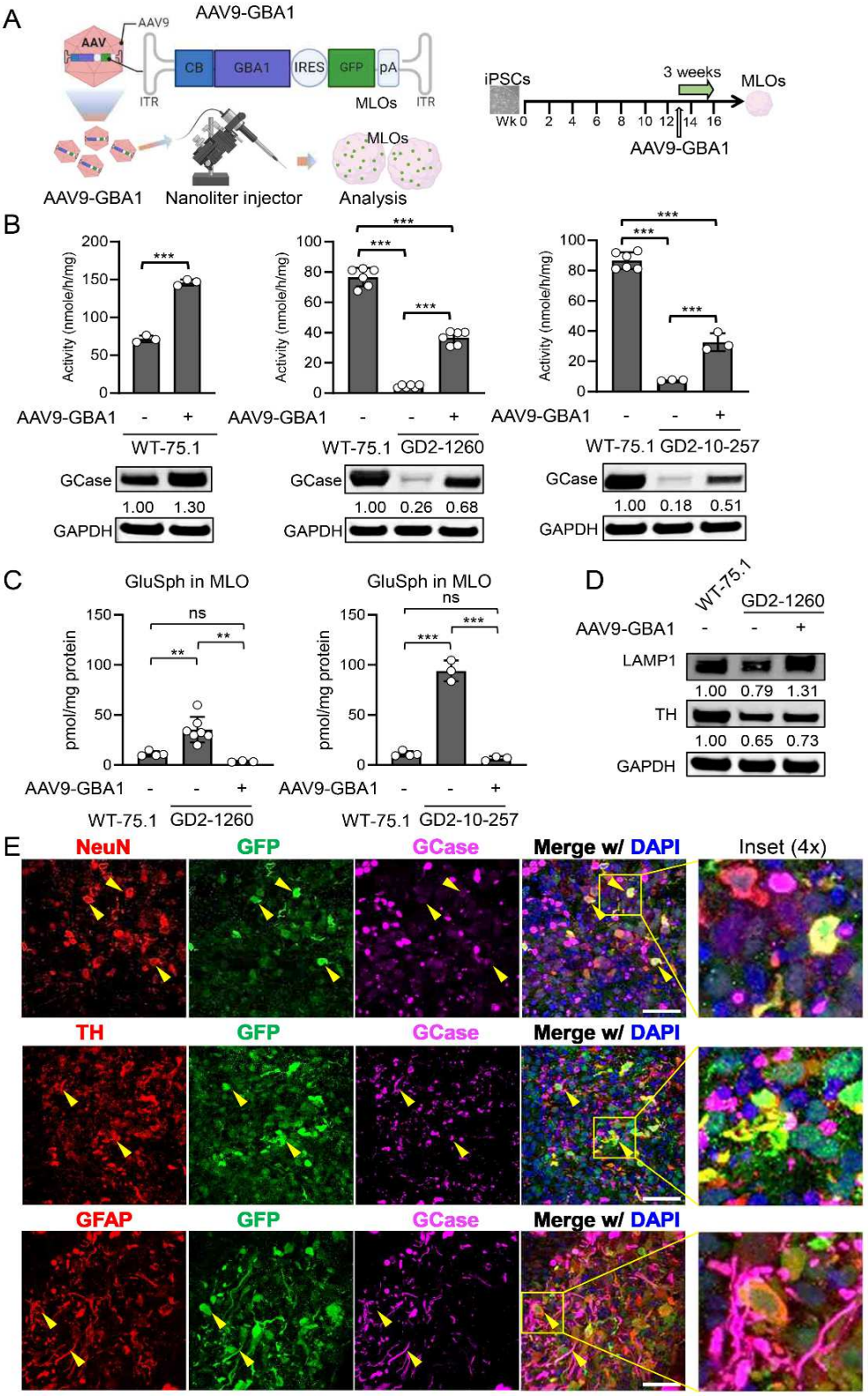
A
AAV9-GBA1
AAV9
AAV
CB
GBA1
IRES
GFP
pA
ITR
MLOs
ITR
AAV9-GBA1
Nanoliter injector
MLOs
Analysis
iPSCs
3 weeks
MLOs
Wk 0 2 4 6 8 10 12 14 16
AAV9-GBA1
B
Activity (nmole/h/mg)
AAV9-GBA1 - +
WT-75.1
GCase
1.00 1.30
GAPDH
AAV9-GBA1 - - +
WT-75.1 GD2-1260
GCase
1.00 0.26 0.68
GAPDH
AAV9-GBA1 - - +
WT-75.1 GD2-10-257
GCase
1.00 0.18 0.51
GAPDH
C
GluSph in MLO
pmol/mg protein
ns
AAV9-GBA1 - - +
WT-75.1 GD2-1260
GluSph in MLO
pmol/mg protein
ns
AAV9-GBA1 - - +
WT-75.1 GD2-10-257
D
WT-75.1
GD2-1260
AAV9-GBA1 - - +
LAMP1
1.00 0.79 1.31
TH
1.00 0.65 0.73
GAPDH
E
NeuN
GFP
GCase
Merge w/ DAPI
Inset (4x)
TH
GFP
GCase
Merge w/ DAPI
GFAP
GFP
GCase
Merge w/ DAPI

917

918 **Figure 6. AAV9-GBA1 gene therapy mitigates disease phenotypes in GD MLOs.**

919 (A) Schematic illustration of AAV9-*GBA1* gene therapy delivery to MLOs using a nanoliter
920 injector. AAV9 vectors carrying the GBA1 gene (AAV9-GBA1) are administered to Wk13 MLOs.
921 The samples were analyzed after 3 weeks of treatment.

922 (B) GCase activity in WT-75.1, GD2-1260, and GD2-10-257 MLOs and AAV9-GBA1 treated
923 MLOs were measured by enzymatic assay. Data are presented as mean ± SEM (3 MLOs pooled,
924 n = 3 to 6 per group). ***$p < 0.001$.

925 (C) GluSph levels in AAV9-GBA1 treated GD and control MLOs were quantified by LC-MS/MS
926 and normalized to total protein. Data are presented as mean ± SEM (3 MLOs pooled, $n \geq 3$ per
927 group). ***$p < 0.001$; ns, not significant.

928 (D) Immunoblot analysis of LAMP1 and TH in WT-75.1 and in GD2-1260 MLOs untreated or
929 treated with AAV9-GBA1. Protein samples were extracted from n=3 MLOs for each group.
930 Protein levels are normalized to WT-75.1 untreated controls (set to 1.0).

931 (E) Transgene expressions (yellow arrows and enlarged insert) in neurons (NeuN), DA neurons
932 (TH) and astrocytes (GFAP) of AAV9-GBA1 treated GD2-1260 MLOs. Scale bar = 50 μm.

933

Fig. 7

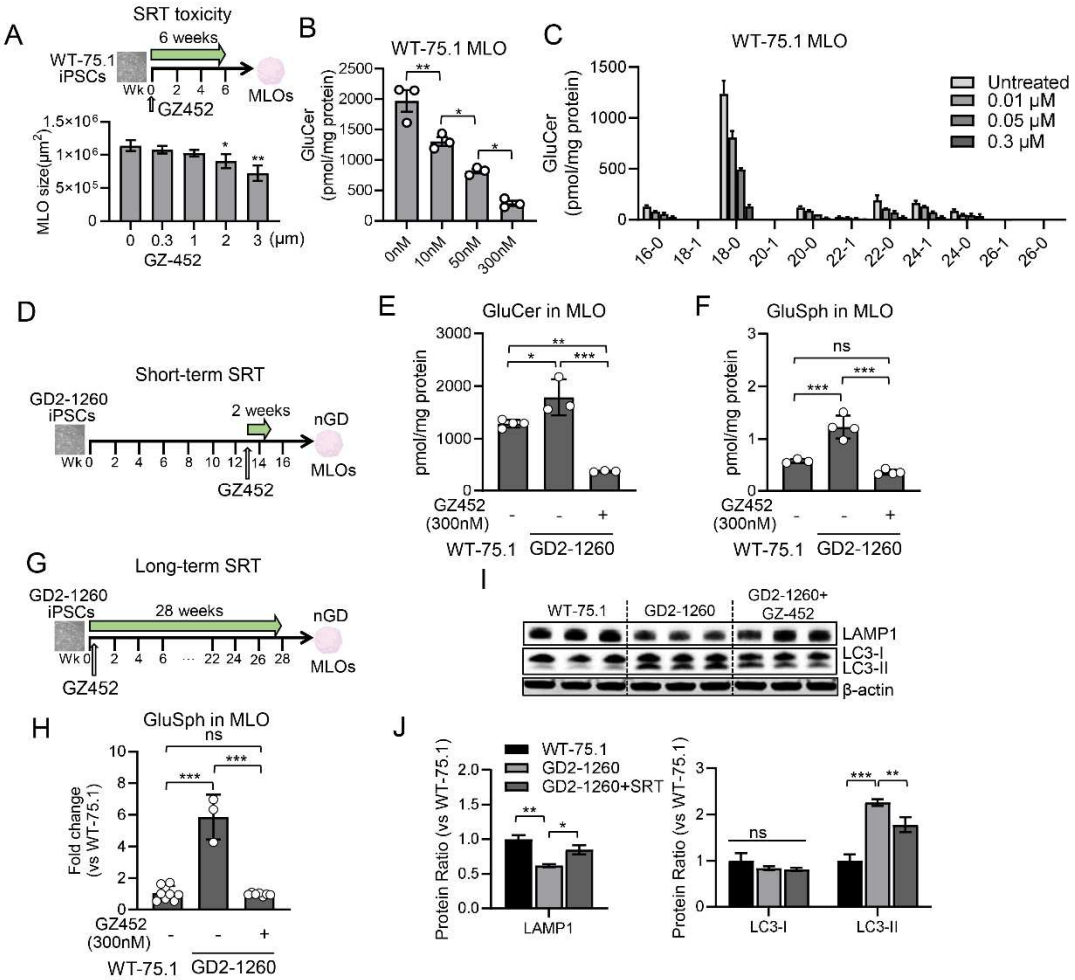

Figure 7. Substrate Reduction Therapy with GZ452 reduces lipid accumulation and improves autophagic and lysosomal abnormalities in GD MLOs.

(A) Assessment of GZ452 tolerated dose in healthy MLO and the effect of GZ452 on organoid growth in WT-75.1 MLOs over 6 weeks. Three MLOs were pooled and n = 3 per concentration.

(B, C) Total GluCer levels (B) and distribution of GluCer species (C) in WT-75.1 MLOs with various doses of GZ452 at Wk6. Three MLOs were pooled and n = 3 per concentration.

(D) Schematic of the experimental timeline for short-term (2 weeks) GZ452 treatment of GD MLOs.

942 (E, F) GluCer (E) and GluSph (F) levels in WT-75.1 and GD2-1260 MLOs at Wk15 under short-
943 term GZ452 treatment. Data were normalized to protein mass.
944 (G) Schematic of the experimental timeline for long-term (28 weeks) GZ452 treatment in GD
945 MLOs.
946 (H) GluSph levels in MLOs at Wk15 under long-term GZ452 treatment. Data were normalized to
947 protein mass.
948 (I) Immunoblot analysis of LAMP1 and LC3-I/II in SRT treated GD2-1260 MLOs for 28 weeks,
949 with β-actin as loading control. Protein samples were extracted from n=3 MLOs for each group.
950 (J) Quantification of LAMP1 and LC3-II/I in MLOs. Protein levels are normalized to WT-75.1
951 untreated controls (set to 1.0).
952 All data presented as mean ± SEM (n = 3~4). *$p < 0.05$; **$p < 0.01$; ns, not significant. One-way
953 ANOVA with Tukey's test.
954

955 **Additional files**

956

957 **Supplementary files**

958 **Supplementary Fig. 1.** Correct L444P mutation in nGD iPSC by CRISPR-Cas9. (A) Single
959 stranded oligonucleotide design. Silent mutations in upper case. Phosphorothioate modified bases
960 (*). (B) Genomic sequence of mutant, wild type and corrected GBA1. Mutated codon highlighted
961 in red. T insertion for point mutation correction highlighted in yellow. PAM highlighted in grey.
962 sgRNA target sequence underlined. (C) DNA electrophoresis gels showing genome editing and
963 clone
964 screening for iso-GD2-1260 (clone #9). (D) Karyotyping of GD2-1260 and CRISPR/Cas9
965 corrected iso-GD2-1260 hiPSCs. Normal karyotype was observed in both hiPSC lines. (E)
966 Relative mRNA expression of genes (OCT4, NANOG and SOX2) required for generating and
967 maintaining hiPSCs pluripotency by quantitative RT-PCR. ns, not significant by One-way ANOVA
968 analysis.

969

970 **Supplementary Fig. 2.** Representative UHPLC-MS/MS chromatograms of GluSph and GluCer
971 species in WT-75.1 and GD2-1260 MLOs. Tissues from Wk 28 MLOs were tested.

972

973 **Supplementary Fig. 3**. Neural rosette formation during MLO maturation were not affected by
974 GBA1 mutation. (A) Cryosections of Wk 6 MLOs derived from WT-75.1, GD2-1260 and isogenic
975 control iso-GD2-1260 hiPSC cells. Sections were stained with antibodies against Ki67 and Sox2
976 and nuclei were costained with DAPI. Scale bar, 100 μm. (B) Quantification of the Sox2+, Ki67+
977 and Sox2+/Ki67+ cells (mean ± SEM; n = 3). ns, not significant by One-way ANOVA analysis.

978

979 **Supplementary Fig. 4**. Restoration of GCase Expression in dopaminergic neuron and astrocytes
980 in SapC-DOPS-fGCase treated nGD MLOs. (A, B) Representative confocal images of GD2-1260
981 (A) and GD2-10-257 MLOs (B) treated with SapC-DOPS-fGCase for 2 weeks, immunostained
982 for GCase (green) and dopaminergic neuron (TH, red) with DAPI (blue) labeling nuclei. (C, D)
983 Representative immunostaining images for GCase (green) and astrocytes (GFAP, red) in GD2-
984 1260 (C) and GD2-10-257 MLOs (D) treated with SapC-DOPS-fGCase. Scale bar, 50 μm. Yellow
985 arrows indicate colocalized GCase in TH+ cells. (E) Immunoblot of TH in Wk 16 and Wk 28 GD2-
986 10-257 MLOs.

987

988 **Supplementary Fig. 5**. Restoration of GCase expression in lysosomal and autophagosomal
989 compartments in SapC-DOPS-fGCase treated nGD MLOs. (A, B) Representative confocal images
990 of GD2-1260 (A) and GD2-10-257 MLOs (B) treated with SapC-DOPS-fGCase for 2 weeks,
991 immunostained for GCase (green) and lysosomal marker LAMP1 (red) with DAPI (blue) labeling
992 nuclei. Yellow arrows indicate colocalized GCase in LAMP1+ compartments. Scale bar, 50 μm.
993 (C, D) Representative confocal images of GD2-1260 (C) and GD2-10-257 MLOs (D) treated with
994 SapC-DOPS-fGCase for 2 weeks, immunostained for GCase (green) and autophagosomal marker
995 LC3B (red) with DAPI (blue) labeling nuclei. Yellow arrows indicate colocalized GCase in LC3B+
996 compartments. Scale bar, 50 μm.

997

998 **Supplementary Fig. 6**. Influence of SRT drug GZ452 on DA neuron differentiation in WT-75.1
999 MLOs. Relative mRNA expression of midbrain markers ASCL1, TH, and PLZF in WT-75.1 at
1000 Wk6 in untreated or treated MLOs with indicated concentrations of GZ452. Relative gene

1001 expression is normalized to untreated control WT-75.1 MLOs (set to 1.0).

1002

1003 **Supplementary Table 1**. Key Resources

1004 **Supplementary Table 2**. Summary of therapeutic modalities on nGD MLOs

1005 **Supplementary Table 3**. Key Dysregulated Pathways

1006

1007

1008 **Data availability**

1009 RNA-seq data generated in this study were deposited in Gene Expression Omnibus (GEO) at

1010 National Institutes of Health (NIH) with accession number GSE303993.

1011

References

1. Grabowski, G.A., Petsko, G.A., and Kolodny, E.H. (2010). Gaucher disease. In The Online Metabolic and Molecular Bases of Inherited Diseases, D. Valle, A. Beaudet, B. Vogelstein, K.W. Kinzler, S.E. Antonarakis, A. Ballabio, C.R. Scriver, W.S. Sly, B. Childs, F. Bunz, et al., eds. (New York: The McGraw-Hill Companies, Inc.).
2. Mignot, C., Gelot, A., Bessieres, B., Daffos, F., Voyer, M., Menez, F., Fallet Bianco, C., Odent, S., Le Duff, D., Loget, P., Fargier, P., et al. (2003). Perinatal-lethal Gaucher disease. American journal of medical genetics. Part A *120A*, 338–344. 10.1002/ajmg.a.20117.
3. Reissner, K., Tayebi, N., Stubblefield, B.K., Koprivica, V., Blitzer, M., Holleran, W., Cowan, T., Almashanu, S., Maddalena, A., Karson, E.M., and Sidransky, E. (1998). Type 2 Gaucher disease with hydrops fetalis in an Ashkenazi Jewish family resulting from a novel recombinant allele and a rare splice junction mutation in the glucocerebrosidase locus. Molecular genetics and metabolism *63*, 281–288. 10.1006/mgme.1998.2675.
4. Burrow, T.A., Sun, Y., Prada, C.E., Bailey, L., Zhang, W., Brewer, A., Wu, S.W., Setchell, K.D.R., Witte, D., Cohen, M.B., and Grabowski, G.A. (2015). CNS, lung, and lymph node involvement in Gaucher disease type 3 after 11 years of therapy: clinical, histopathologic, and biochemical findings. Molecular genetics and metabolism *114*, 233–241. 10.1016/j.ymgme.2014.08.011.
5. Wong, K., Sidransky, E., Verma, A., Mixon, T., Sandberg, G.D., Wakefield, L.K., Morrison, A., Lwin, A., Colegial, C., Allman, J.M., and Schiffmann, R. (2004). Neuropathology provides clues to the pathophysiology of Gaucher disease. Molecular genetics and metabolism *82*, 192–207. 10.1016/j.ymgme.2004.04.011.
6. Conradi, N.G., Sourander, P., Nilsson, O., Svennerholm, L., and Erikson, A. (1984). Neuropathology of the Norrbottnian type of Gaucher disease. Morphological and biochemical studies. Acta neuropathologica *65*, 99–109.
7. Enquist, I.B., Lo Bianco, C., Ooka, A., Nilsson, E., Mansson, J.E., Ehinger, M., Richter, J., Brady, R.O., Kirik, D., and Karlsson, S. (2007). Murine models of acute neuronopathic Gaucher disease. Proceedings of the National Academy of Sciences of the United States of America *104*, 17483–17488. 10.1073/pnas.0708086104.
8. Vardi, A., Zigdon, H., Meshcheriakova, A., Klein, A.D., Yaacobi, C., Eilam, R., Kenwood, B.M., Rahim, A.A., Massaro, G., Merrill, A.H., Jr., Vitner, E.B., et al. (2016). Delineating pathological pathways in a chemically induced mouse model of Gaucher disease. J Pathol *239*, 496–509. 10.1002/path.4751.
9. Xu, Y.H., Reboulet, R., Quinn, B., Huelsken, J., Witte, D., and Grabowski, G.A. (2008). Dependence of reversibility and progression of mouse neuronopathic Gaucher disease on acid beta-glucosidase residual activity levels. Molecular genetics and metabolism *94*, 190–203. 10.1016/j.ymgme.2008.01.013.
10. Xu, Y.H., Quinn, B., Witte, D., and Grabowski, G.A. (2003). Viable mouse models of acid beta-glucosidase deficiency: the defect in Gaucher disease. Am J Pathol *163*, 2093–2101. 10.1016/s0002-9440(10)63566-3.
11. Sun, Y., Liou, B., Ran, H., Skelton, M.R., Williams, M.T., Vorhees, C.V., Kitatani, K., Hannun, Y.A., Witte, D.P., Xu, Y.H., and Grabowski, G.A. (2010). Neuronopathic Gaucher disease in the mouse: viable combined selective saposin C deficiency and mutant glucocerebrosidase (V394L) mice with glucosylsphingosine and glucosylceramide accumulation and progressive neurological deficits. Human molecular genetics *19*, 1088–

1097. 10.1093/hmg/ddp580.
12. Qi, X., Leonova, T., and Grabowski, G.A. (1994). Functional human saposins expressed in Escherichia coli. Evidence for binding and activation properties of saposins C with acid beta-glucosidase. J Biol Chem *269*, 16746–16753.
13. Dasgupta, N., Xu, Y.H., Li, R., Peng, Y., Pandey, M.K., Tinch, S.L., Liou, B., Inskeep, V., Zhang, W., Setchell, K.D., Keddache, M., et al. (2015). Neuronopathic Gaucher disease: dysregulated mRNAs and miRNAs in brain pathogenesis and effects of pharmacologic chaperone treatment in a mouse model. Human molecular genetics *24*, 7031–7048. 10.1093/hmg/ddv404.
14. Liu, Y., Suzuki, K., Reed, J.D., Grinberg, A., Westphal, H., Hoffmann, A., Doring, T., Sandhoff, K., and Proia, R.L. (1998). Mice with type 2 and 3 Gaucher disease point mutations generated by a single insertion mutagenesis procedure. Proceedings of the National Academy of Sciences of the United States of America *95*, 2503–2508. 10.1073/pnas.95.5.2503.
15. Pasmanik-Chor, M., Laadan, S., Elroy-Stein, O., Zimran, A., Abrahamov, A., Gatt, S., and Horowitz, M. (1996). The glucocerebrosidase D409H mutation in Gaucher disease. Biochemical and molecular medicine *59*, 125–133. 10.1006/bmme.1996.0077.
16. Grabowski, G.A., Zimran, A., and Ida, H. (2015). Gaucher disease types 1 and 3: Phenotypic characterization of large populations from the ICGG Gaucher Registry. American journal of hematology *90 Suppl 1*, S12–18. 10.1002/ajh.24063.
17. Birtele, M., Lancaster, M., and Quadrato, G. (2025). Modelling human brain development and disease with organoids. Nat Rev Mol Cell Biol *26*, 389–412. 10.1038/s41580-024-00804-1.
18. Di Lullo, E., and Kriegstein, A.R. (2017). The use of brain organoids to investigate neural development and disease. Nature reviews. Neuroscience *18*, 573–584. 10.1038/nrn.2017.107.
19. Raja, W.K., Mungenast, A.E., Lin, Y.T., Ko, T., Abdurrob, F., Seo, J., and Tsai, L.H. (2016). Self-Organizing 3D Human Neural Tissue Derived from Induced Pluripotent Stem Cells Recapitulate Alzheimer's Disease Phenotypes. PLoS One *11*, e0161969. 10.1371/journal.pone.0161969.
20. Lancaster, M.A., Renner, M., Martin, C.A., Wenzel, D., Bicknell, L.S., Hurles, M.E., Homfray, T., Penninger, J.M., Jackson, A.P., and Knoblich, J.A. (2013). Cerebral organoids model human brain development and microcephaly. Nature *501*, 373–379. 10.1038/nature12517.
21. Smits, L.M., Reinhardt, L., Reinhardt, P., Glatza, M., Monzel, A.S., Stanslowsky, N., Rosato-Siri, M.D., Zanon, A., Antony, P.M., Bellmann, J., Nicklas, S.M., et al. (2019). Modeling Parkinson's disease in midbrain-like organoids. NPJ Parkinson's disease *5*, 5. 10.1038/s41531-019-0078-4.
22. Allende, M.L., Cook, E.K., Larman, B.C., Nugent, A., Brady, J.M., Golebiowski, D., Sena-Esteves, M., Tifft, C.J., and Proia, R.L. (2018). Cerebral organoids derived from Sandhoff disease-induced pluripotent stem cells exhibit impaired neurodifferentiation. J Lipid Res *59*, 550–563. 10.1194/jlr.M081323.
23. Latour, Y.L., Yoon, R., Thomas, S.E., Grant, C., Li, C., Sena-Esteves, M., Allende, M.L., Proia, R.L., and Tifft, C.J. (2019). Human GLB1 knockout cerebral organoids: A model system for testing AAV9-mediated GLB1 gene therapy for reducing GM1 ganglioside storage in GM1 gangliosidosis. Mol Genet Metab Rep *21*, 100513.

10.1016/j.ymgmr.2019.100513.
24. Jo, J., Yang, L., Tran, H.D., Yu, W., Sun, A.X., Chang, Y.Y., Jung, B.C., Lee, S.J., Saw, T.Y., Xiao, B., Khoo, A.T.T., et al. (2021). Lewy Body-like Inclusions in Human Midbrain Organoids Carrying Glucocerebrosidase and alpha-Synuclein Mutations. Ann Neurol *90*, 490–505. 10.1002/ana.26166.
25. Goker-Alpan, O., and Ivanova, M.M. (2024). Neuronopathic Gaucher disease: Rare in the West, common in the East. J Inherit Metab Dis *47*, 917–934. 10.1002/jimd.12749.
26. Farfel-Becker, T., Vitner, E.B., Kelly, S.L., Bame, J.R., Duan, J., Shinder, V., Merrill, A.H., Jr., Dobrenis, K., and Futerman, A.H. (2014). Neuronal accumulation of glucosylceramide in a mouse model of neuronopathic Gaucher disease leads to neurodegeneration. Human molecular genetics *23*, 843–854. 10.1093/hmg/ddt468.
27. Jones, E.E., Zhang, W., Zhao, X., Quiason, C., Dale, S., Shahidi-Latham, S., Grabowski, G.A., Setchell, K.D.R., Drake, R.R., and Sun, Y. (2017). Tissue Localization of Glycosphingolipid Accumulation in a Gaucher Disease Mouse Brain by LC-ESI-MS/MS and High-Resolution MALDI Imaging Mass Spectrometry. SLAS Discov *22*, 1218–1228. 10.1177/2472555217719372.
28. Xu, Y.H., Xu, K., Sun, Y., Liou, B., Quinn, B., Li, R.H., Xue, L., Zhang, W., Setchell, K.D., Witte, D., and Grabowski, G.A. (2014). Multiple pathogenic proteins implicated in neuronopathic Gaucher disease mice. Human molecular genetics *23*, 3943–3957. 10.1093/hmg/ddu105.
29. Sun, Y., Florer, J., Mayhew, C.N., Jia, Z., Zhao, Z., Xu, K., Ran, H., Liou, B., Zhang, W., Setchell, K.D., Gu, J., et al. (2015). Properties of neurons derived from induced pluripotent stem cells of Gaucher disease type 2 patient fibroblasts: potential role in neuropathology. PLoS One *10*, e0118771. 10.1371/journal.pone.0118771.
30. Awad, O., Panicker, L.M., Deranieh, R.M., Srikanth, M.P., Brown, R.A., Voit, A., Peesay, T., Park, T.S., Zambidis, E.T., and Feldman, R.A. (2017). Altered Differentiation Potential of Gaucher's Disease iPSC Neuronal Progenitors due to Wnt/beta-Catenin Downregulation. Stem Cell Reports *9*, 1853–1867. 10.1016/j.stemcr.2017.10.029.
31. Kwak, T.H., Kang, J.H., Hali, S., Kim, J., Kim, K.P., Park, C., Lee, J.H., Ryu, H.K., Na, J.E., Jo, J., Je, H.S., et al. (2020). Generation of homogeneous midbrain organoids with in vivo-like cellular composition facilitates neurotoxin-based Parkinson's disease modeling. Stem cells *38*, 727–740. 10.1002/stem.3163.
32. Jo, J., Xiao, Y., Sun, A.X., Cukuroglu, E., Tran, H.D., Goke, J., Tan, Z.Y., Saw, T.Y., Tan, C.P., Lokman, H., Lee, Y., et al. (2016). Midbrain-like Organoids from Human Pluripotent Stem Cells Contain Functional Dopaminergic and Neuromelanin-Producing Neurons. Cell stem cell *19*, 248–257. 10.1016/j.stem.2016.07.005.
33. Ran, F.A., Hsu, P.D., Wright, J., Agarwala, V., Scott, D.A., and Zhang, F. (2013). Genome engineering using the CRISPR-Cas9 system. Nat Protoc *8*, 2281–2308. 10.1038/nprot.2013.143.
34. Chen, B., Gilbert, L.A., Cimini, B.A., Schnitzbauer, J., Zhang, W., Li, G.W., Park, J., Blackburn, E.H., Weissman, J.S., Qi, L.S., and Huang, B. (2013). Dynamic imaging of genomic loci in living human cells by an optimized CRISPR/Cas system. Cell *155*, 1479–1491. 10.1016/j.cell.2013.12.001.
35. Horowitz, M., Wilder, S., Horowitz, Z., Reiner, O., Gelbart, T., and Beutler, E. (1989). The human glucocerebrosidase gene and pseudogene: structure and evolution. Genomics *4*, 87–96. 10.1016/0888-7543(89)90319-4.

36. Woo, E.G., Tayebi, N., and Sidransky, E. (2021). Next-Generation Sequencing Analysis of GBA1: The Challenge of Detecting Complex Recombinant Alleles. Front Genet *12*, 684067. 10.3389/fgene.2021.684067.
37. Hsu, P.D., Scott, D.A., Weinstein, J.A., Ran, F.A., Konermann, S., Agarwala, V., Li, Y., Fine, E.J., Wu, X., Shalem, O., Cradick, T.J., et al. (2013). DNA targeting specificity of RNA-guided Cas9 nucleases. Nature Biotechnology *31*, 827–832. 10.1038/nbt.2647.
38. Sun, Y., Liou, B., Chu, Z., Fannin, V., Blackwood, R., Peng, Y., Grabowski, G.A., Davis, H.W., and Qi, X. (2020). Systemic enzyme delivery by blood-brain barrier-penetrating SapC-DOPS nanovesicles for treatment of neuronopathic Gaucher disease. EBioMedicine *55*, 102735. 10.1016/j.ebiom.2020.102735.
39. Zhao, S., Chu, Z., Blanco, V.M., Nie, Y., Hou, Y., and Qi, X. (2015). SapC-DOPS nanovesicles as targeted therapy for lung cancer. Mol Cancer Ther *14*, 491–498. 10.1158/1535-7163.MCT-14-0661.
40. Marshall, J., Sun, Y., Bangari, D.S., Budman, E., Park, H., Nietupski, J.B., Allaire, A., Cromwell, M.A., Wang, B., Grabowski, G.A., Leonard, J.P., et al. (2016). CNS-accessible Inhibitor of Glucosylceramide Synthase for Substrate Reduction Therapy of Neuronopathic Gaucher Disease. Mol Ther *24*, 1019–1029. 10.1038/mt.2016.53.
41. Sun, Y., Zhang, W., Xu, Y.H., Quinn, B., Dasgupta, N., Liou, B., Setchell, K.D., and Grabowski, G.A. (2013). Substrate compositional variation with tissue/region and Gba1 mutations in mouse models--implications for Gaucher disease. PLoS One *8*, e57560. 10.1371/journal.pone.0057560.
42. Zhang, W., Oehrle, M., Prada, C.E., Schwartz, I.V.D., Chutipongtanate, S., Wattanasirichaigoon, D., Inskeep, V., Dai, M., Pan, D., Sun, Y., and Setchell, K.D.R. (2017). A convenient approach to facilitate monitoring Gaucher disease progression and therapeutic response. The Analyst *142*, 3380–3387. 10.1039/c7an00938k.
43. Zhao, X., Lin, Y., Liou, B., Fu, W., Jian, J., Fannie, V., Zhang, W., Setchell, K.D.R., Grabowski, G.A., Sun, Y., and Liu, C.J. (2023). PGRN deficiency exacerbates, whereas a brain penetrant PGRN derivative protects, GBA1 mutation-associated pathologies and diseases. Proceedings of the National Academy of Sciences of the United States of America *120*, e2210442120. 10.1073/pnas.2210442120.
44. Love, M.I., Huber, W., and Anders, S. (2014). Moderated estimation of fold change and dispersion for RNA-seq data with DESeq2. Genome Biol *15*, 550. 10.1186/s13059-014-0550-8.
45. Sherman, B.T., Hao, M., Qiu, J., Jiao, X., Baseler, M.W., Lane, H.C., Imamichi, T., and Chang, W. (2022). DAVID: a web server for functional enrichment analysis and functional annotation of gene lists (2021 update). Nucleic Acids Res *50*, W216–W221. 10.1093/nar/gkac194.
46. Dai, M., Lin, Y., El-Amouri, S.S., Kohls, M., and Pan, D. (2018). Comprehensive evaluation of blood-brain barrier-forming micro-vasculatures: Reference and marker genes with cellular composition. PLoS One *13*, e0197379. 10.1371/journal.pone.0197379.
47. Prakash, N., and Wurst, W. (2006). Genetic networks controlling the development of midbrain dopaminergic neurons. J Physiol *575*, 403–410. 10.1113/jphysiol.2006.113464.
48. Green, D., Whitener, A.E., Mohanty, S., and Lekven, A.C. (2015). Vertebrate nervous system posteriorization: Grading the function of Wnt signaling. Dev Dyn *244*, 507–512. 10.1002/dvdy.24230.
49. Ryckman, A.E., Brockhausen, I., and Walia, J.S. (2020). Metabolism of

Glycosphingolipids and Their Role in the Pathophysiology of Lysosomal Storage Disorders. Int J Mol Sci *21*. 10.3390/ijms21186881.

50. Srikanth, M.P., Jones, J.W., Kane, M., Awad, O., Park, T.S., Zambidis, E.T., and Feldman, R.A. (2021). Elevated glucosylsphingosine in Gaucher disease induced pluripotent stem cell neurons deregulates lysosomal compartment through mammalian target of rapamycin complex 1. Stem Cells Transl Med *10*, 1081–1094. 10.1002/sctm.20-0386.
51. Mato-Blanco, X., Kim, S.K., Jourdon, A., Ma, S., Choi, S.H., Giani, A.M., Paredes, M.I., Tebbenkamp, A.T.N., Liu, F., Duque, A., Vaccarino, F.M., et al. (2025). Early developmental origins of cortical disorders modeled in human neural stem cells. Nat Commun *16*, 6347. 10.1038/s41467-025-61316-w.
52. Ba, R., Yang, L., Zhang, B., Jiang, P., Ding, Z., Zhou, X., Yang, Z., and Zhao, C. (2023). FOXG1 drives transcriptomic networks to specify principal neuron subtypes during the development of the medial pallium. Sci Adv *9*, eade2441. 10.1126/sciadv.ade2441.
53. Ortiz, A., Ayhan, F., Khandelwal, N., Outland, E., Jankovic, M., Harper, M., and Konopka, G. (2025). Cell-type-specific roles of FOXP1 in the excitatory neuronal lineage during early neocortical murine development. Cell Rep *44*, 115384. 10.1016/j.celrep.2025.115384.
54. Peng, Y., Liou, B., Lin, Y., Mayhew, C.N., Fleming, S.M., and Sun, Y. (2023). iPSC-derived neural precursor cells engineering GBA1 recovers acid beta-glucosidase deficiency and diminishes alpha-synuclein and neuropathology. Mol Ther Methods Clin Dev *29*, 185–201. 10.1016/j.omtm.2023.03.007.
55. Brown, R.A., Voit, A., Srikanth, M.P., Thayer, J.A., Kingsbury, T.J., Jacobson, M.A., Lipinski, M.M., Feldman, R.A., and Awad, O. (2019). mTOR hyperactivity mediates lysosomal dysfunction in Gaucher's disease iPSC-neuronal cells. Dis Model Mech *12*. 10.1242/dmm.038596.
56. Panicker, L.M., Miller, D., Park, T.S., Patel, B., Azevedo, J.L., Awad, O., Masood, M.A., Veenstra, T.D., Goldin, E., Stubblefield, B.K., Tayebi, N., et al. (2012). Induced pluripotent stem cell model recapitulates pathologic hallmarks of Gaucher disease. Proceedings of the National Academy of Sciences of the United States of America *109*, 18054–18059. 10.1073/pnas.1207889109.
57. Comper, F., Miranda, C.J., Liou, B., Dodev, T., Jeyakumar, J.M., Canavese, M., Cocita, C., Khoshrou, K., Tiscornia, G., Chisari, E., Stotter, E., et al. (2025). FLT201, a novel liver-directed AAV gene therapy candidate for Gaucher disease type 1. Mol Ther *33*, 3789–3807. 10.1016/j.ymthe.2025.05.003.
58. Hughes, D.A., and Ferrante, F. (2023). GALILEO-1: A Phase I/II safety and efficacy study of FLT201 gene therapy for Gaucher disease type 1. Future Rare Diseases *3*, FRD35.
59. Al-Zaidy, S., Pickard, A.S., Kotha, K., Alfano, L.N., Lowes, L., Paul, G., Church, K., Lehman, K., Sproule, D.M., Dabbous, O., Maru, B., et al. (2019). Health outcomes in spinal muscular atrophy type 1 following AVXS-101 gene replacement therapy. Pediatr Pulmonol *54*, 179–185. 10.1002/ppul.24203.
60. Drag, S., Dotiwala, F., and Upadhyay, A.K. (2023). Gene Therapy for Retinal Degenerative Diseases: Progress, Challenges, and Future Directions. Invest Ophthalmol Vis Sci *64*, 39. 10.1167/iovs.64.7.39.
61. Aerts, J.M., Hollak, C.E., Boot, R.G., Groener, J.E., and Maas, M. (2006). Substrate reduction therapy of glycosphingolipid storage disorders. J Inherit Metab Dis *29*, 449–456. 10.1007/s10545-006-0272-5.
62. Scott, L.J. (2015). Eliglustat: A Review in Gaucher Disease Type 1. Drugs *75*, 1669–1678.

10.1007/s40265-015-0468-9.

63. Schiffmann, R., Mengel, E., Wallace, M., Rochmann, C., Turnbull, J., Krupnick, R., Gwaltney, C., Pulikottil-Jacob, R., Batsu, I., Zheng, R., and Hamed, A. (2024). Qualitative Study of the Patient Experience with Venglustat for Gaucher Disease Type 3 in a Phase 2 Open-Label, Multicenter, Multinational Study (LEAP). Adv Ther *41*, 2907–2923. 10.1007/s12325-024-02881-2.

64. Zagare, A., Barmpa, K., Smajic, S., Smits, L.M., Grzyb, K., Grunewald, A., Skupin, A., Nickels, S.L., and Schwamborn, J.C. (2022). Midbrain organoids mimic early embryonic neurodevelopment and recapitulate LRRK2-p.Gly2019Ser-associated gene expression. Am J Hum Genet *109*, 311–327. 10.1016/j.ajhg.2021.12.009.

65. Grace, M.E., Berg, A., He, G.S., Goldberg, L., Horowitz, M., and Grabowski, G.A. (1991). Gaucher disease: heterologous expression of two alleles associated with neuronopathic phenotypes. Am J Hum Genet *49*, 646–655.

66. Ron, I., Dagan, A., Gatt, S., Pasmanik-Chor, M., and Horowitz, M. (2005). Use of fluorescent substrates for characterization of Gaucher disease mutations. Blood Cells Mol Dis *35*, 57–65. 10.1016/j.bcmd.2005.03.006.

67. Peng, Y., Liou, B., Lin, Y., Fannin, V., Zhang, W., Feldman, R.A., Setchell, K.D.R., Grabowski, G.A., and Sun, Y. (2021). Substrate Reduction Therapy Reverses Mitochondrial, mTOR, and Autophagy Alterations in a Cell Model of Gaucher Disease. Cells *10*. 10.3390/cells10092286.

68. Cakir, B., Tanaka, Y., Kiral, F.R., Xiang, Y., Dagliyan, O., Wang, J., Lee, M., Greaney, A.M., Yang, W.S., duBoulay, C., Kural, M.H., et al. (2022). Expression of the transcription factor PU.1 induces the generation of microglia-like cells in human cortical organoids. Nat Commun *13*, 430. 10.1038/s41467-022-28043-y.

69. Sabate-Soler, S., Nickels, S.L., Saraiva, C., Berger, E., Dubonyte, U., Barmpa, K., Lan, Y.J., Kouno, T., Jarazo, J., Robertson, G., Sharif, J., et al. (2022). Microglia integration into human midbrain organoids leads to increased neuronal maturation and functionality. Glia *70*, 1267–1288. 10.1002/glia.24167.